

Velocities and relative amount of material ejected from Comet 9P/Tempel 1 after the Deep Impact collision

Sergei I. Ipatov ^{a,1,*} and Michael F. A'Hearn ^b

^a Department of Physics, Catholic University of America, Washington DC, 20064, USA

* Corresponding Author E-mail address: siipatov@hotmail.com

^b Department of Astronomy, University of Maryland, College Park MD, 20740, U.S.A.

¹ The work was initiated at University of Maryland

Submitted to Icarus after revision of reviewer's remarks

Abstract

Time variations of velocities and relative amount of material ejected from Comet 9P/Tempel 1 are studied based on analysis of the images made by Deep Impact (DI) cameras during the first 13 minutes after the collision of the DI impactor with the comet. The rate of production of observed ejected material and velocities considered correspond mainly to small (with diameter $d < 3 \mu\text{m}$) icy particles. The rate had a peak at ejection time $t_e \sim 0.6$ s. At $1 < t_e < 3$ s and $8 < t_e < 40$ s the estimated rate of ejection was essentially greater than for theoretical monotonic exponential decrease. Such difference was caused by that the impact was a trigger of an outburst. At the time $t_e \sim 10$ s corresponding to a local maximum of ejection rate, the direction from the place of ejection to the brightest pixel quickly changed by about 50° , a considerable excessive ejection (rays of ejected material) to a few directions began, and typical projections of velocities onto the plane perpendicular to the line of sight were $\sim 100\text{-}200 \text{ m s}^{-1}$. A sharp (by a factor of 3) decrease of the ejection rate at $t_e \sim 60$ s could be caused by a decrease of the outburst. The outburst continued after 60 s because the rays were still observed in images at $t \sim 500\text{-}700$ s. Our studies do not contradict to a continuous ejection of material during at least 10 minutes after the collision. As a first approximation, the characteristic velocity of ejection at $1 \text{ s} < t_e < 60 \text{ s}$ can be considered to be proportional to $t_e^{-0.75}$ or $t_e^{-0.7}$, but the decrease of velocity could differ from this exponential dependence.

Key words: Comets; Comet 9P/Tempel 1; Comets, Dust

1. Introduction

On July 4, 2005 370 kg impactor collided with Comet 9P/Tempel 1 at velocity of 10.3 km s^{-1} (A'Hearn et al., 2005). It was an oblique impact, and the angle above the horizon was about $20\text{-}35^\circ$. Evolution of the cloud of ejected material was observed by Deep Impact (DI) cameras, by space telescopes (e.g., Rosetta, Hubble Space Telescope, Chandra, Spitzer), and by over 80 observatories on the Earth. Ejections similar to the DI ejection can take place when a small celestial body collides with a comet at a high velocity. Therefore, studies of the ejection of material after the DI impact are important for understanding the collisional processes in the solar system.

1.1. Velocities of ejected material

Velocities of ejected dust particles studied in previous publications utilized ground-based observations and observations made by spacecraft other than Deep Impact. The values of the projection of the velocity v_{le} of the leading edge of the dust cloud of ejected material onto the plane perpendicular to the line of sight at several moments of time and of the mass of ejected material obtained at different observations by different authors are presented in Table 1. The velocity of the particles that dominate the cross-section is considered. The values of v_{le} were $\sim 110\text{-}125 \text{ m s}^{-1}$, $150\text{-}200 \text{ m s}^{-1}$, 230 m s^{-1} , $200\text{-}260 \text{ m s}^{-1}$, and 150 m s^{-1} for observations made 1-2 h, 4 h, 15 h, 20-24 h, and 40 h after the impact. Observed velocities of gas were greater than those of dust, and gas could accelerate dust particles. Jehin et al. (2006) obtained that the total CN flux reaches its maximum $96 (\pm 10)$ min after the impact. It may explain the growth of v_{le} after the first hour. After sublimation of ejected ice, the dust is accelerated by collisions with the water molecules. This acceleration can explain why the maximum velocities of v_{le} were observed 15-24 h after impact.

[Table 1]

1.2. Analysis of images made by DI cameras

In contrast to the papers that analyzed ground-based observations and observations made by spacecraft other than DI, in the present paper we obtain similar estimates of the projected velocity v_{le} of the leading edge of the cloud of ejected material based on various images made by DI cameras during the first 13 min. Analyzing three images made by the DI camera at time $t \sim 8\text{-}15 \text{ s}$, Ipatov and A'Hearn (2006) concluded that the projection of velocity of the brightest material onto the plane perpendicular to the line of sight was $\sim 100 \text{ m s}^{-1}$.

The images made by the DI spacecraft during the first second after the impact and at later time were presented and discussed by A'Hearn et al. (2005), Ernst et al. (2006), Melosh (2006), Ernst and Schultz (2007), Schultz et al. (2007), and other scientists. In contrast to the papers cited above, our studies are based on analysis of levels of brightness in DI images. We discuss the amount of material and typical velocities of particles ejected at various times, mainly after that initial, fast puff of hot material. For studies of such amounts and velocities, other authors used other observations, theoretical models, and laboratory experiments. Their results are discussed below.

1.3. Total mass and sizes of ejected particles

Measurements based on observations in the first hour or two are likely dominated by icy particles, and the amount of ice ejected was about $4.5 \times 10^6 - 9 \times 10^6 \text{ kg}$ (Keller et al., 2005; Küppers et al., 2005). Observations of H_2O and OH set a pretty firm lower limit of $5 \times 10^6 \text{ kg}$ just in the ice (A'Hearn, 2007; A'Hearn and Combi, 2007). The total mass of

ejected dust particles with diameter d less than 2 μm , 2.8 μm , 20 μm , and 200 μm was estimated by different authors (see Table 1) to be about $7.3 \times 10^4 - 4.4 \times 10^5$, $1.5 \times 10^5 - 1.6 \times 10^5$, $5.6 \times 10^5 - 8.5 \times 10^5$, and $10^6 - 1.4 \times 10^7$ kg, respectively. In the papers by Lisse et al. (2006), Schleicher et al. (2006), and Meech et al. (2005), maximum in emitted particle surface area was in the 2-10, 1-5, 1-2 μm particle diameter range, respectively. Spectral modeling showed (Sunshine, et al. 2007) that the water ice in the ejecta from Comet Tempel 1 was dominated by 1 ± 1 μm diameter, pure particles, which are smaller than dust particles (2-10 μm). Jorda et al. (2007) concluded that particles with $d < 2.8$ μm represent more than 80% of the cross-section of the observed dust cloud. The results cited above show that velocities discussed in our paper correspond mainly to particles with $d < 3$ μm , which probably constitute not more than 7% of the total ejected material.

1.4. Relation between brightening rate and ejected mass

Meech et al. (2005) concluded that from impact to 1 min after, the comet brightened sharply. Then for the next 6 min, the brightening rate was more gradual. However, at 7 min after impact, the brightening rate increased again, although not as steeply as at first. This rate remained constant for the next 10 to 15 min, at which point the comet's flux began to level off. In the smallest apertures (radius ≈ 1 arc sec), the flux then began to decrease again ~ 45 min after impact. Observations made in the Naval Observatory Flagstaff Station showed (A.K.B. Monet, private communication, 2007) that there were two episodes of rapid brightening – (1) during the first three minutes after the impact and (2) from 8th to 18th minute after the impact. Barber et al. (2007), Keller et al. (2007), and Sugita et al. (2005, 2006) obtained a steady increase in the visible flux from the comet until it reached a maximum around 35 min, 40 min, and an hour post-impact, respectively. The brightness monotonically decreased thereafter. The increase of brightness takes longer than the estimated crater formation time (3-6 min, Schultz et al., 2005).

Since the icy particles may be more highly reflective than the refractory particles, they could dominate the velocities that we are measuring. Spectra by Sunshine et al. (2007) imply that relatively pure ice grains are present, while very preliminary measurements of the albedo of the grains by King et al. (2007) show high albedo in particles of the early ejection. Küppers et al. (2005) and Keller et al. (2007) supposed that the relation between flux and ejected mass may be non-linear, either because increasing optical depth of the impact ejecta limits the flux from newly produced material or because the size distribution of the ejecta changes with time. In their opinion, the probable cause of the long-lasting brightness increase is sublimation and fragmentation of icy particles within the first hour after the impact. On the other hand, Cohran et al. (2007) concluded that size distribution of particles was not changed during the first two days after the impact (as they saw no change in the color of the dust) and grains usually did not fragment in the coma.

The above discussion shows that flux may not depend linearly on the ejected mass and that in the present paper we probably study mainly velocities of icy particles, which are larger than velocities of typical crater ejecta.

1.5. Cone of ejected material

Koschny and Grün (2001) performed impact experiments at velocities between 0.9 and 11.4 km s⁻¹. They obtained that for normal incidence, the total mass ejected at a given angle can be approximated by a Gaussian distribution with a maximum at $\varphi \approx 70^\circ$ to

the target surface. High-angle ejecta plume at $t < 100$ s was predicted by Schultz et al. (2005). They also mentioned that at $t > 200$ s low-velocity components return to the crater. Typical angles of ejection change (mainly increase) with time (Schultz et al., 2007). In most models considered by Holsapple and Housen (2007), ejecta mass with velocity v was proportional to $v^{-1.23}$. This is in accordance with the proportionality to $v^{-1.25}$ obtained by Petit and Farinella (1993). Maximum velocities of ejected particles are considered to be approximately proportional to $d^{1/3}$ (Koschny and Grün, 2001; Jorda et al., 2007).

1.6. Problems considered in different sections

More detailed Introduction can be found in the initial version of the paper on <http://arxiv.org/abs/0810.1294>. In Section 2 we discuss images and contours of fixed brightness that are considered in our paper, and time variations of maximum brightness and of location of the brightest pixel in an image. Besides the above discussion, this section can be interesting to those scientists who work with DI images (or may be with images made by some other spacecraft) because sometimes while comparing images one must take into account the exposure time, saturated pixels, cosmic ray signatures, and some other factors. If one works with DI files from the website, not taking into account the above factors, he can get wrong results. For example, due to not ideal calibration, maximum brightness on images made at different exposure times, but at approximately the same time, can differ by tens of percent (such difference was taken into account e.g. for construction of Figs. 2 and 11). In Section 3 we discuss ejection of material observed during the first 3 seconds. Based on analysis of DI images, in Section 4 we estimate typical velocities of ejected material at several moments of time. These estimates are used in Section 5 for construction of our models for calculation of time variations of rates and velocities of ejection. In Sections 6 and 8 the time variations are studied and compared with those obtained for theoretical models and at experiments. Readers who want to have a quick look on the results of our studies of ejection rates and velocities can read only these two sections. Rays of ejected material are studied in Section 7. If it is not mentioned specially, below we consider projections of velocities onto the plane perpendicular to a line of sight, but not real velocities.

2. Images considered, contours of fixed brightness, and brightest pixels

2.1. Images considered

For this study we use reversibly calibrated (RADREV) images from both cameras on the Deep Impact flyby spacecraft. The data are available at the Small Bodies Node of the Planetary Data System¹ together with a discussion of the calibration procedures. In Table 2 we describe several series of images considered. In each series, the total integration time and the number of pixels in an image were the same. At the time of impact, both cameras were taking images as rapidly as possible in a continuous sequence. Beginning between 5 and 10 s after impact, the spacing between images gradually increased, and we consider images taken up to 13 min after impact. For the maximum-speed images, the range is essentially constant, so all images can be treated as having the same scale, with the Medium Resolution Instrument (MRI) having a scale of $P_{\text{MRI}}=87$ meters per pixel and High Resolution Instrument (HRI) having a scale 5 times smaller, or 17 m per pixel. The scale is proportional to the distance R between the cameras and the

¹ http://pdssbn.astro.umd.edu/holdings/dif-c-mri-3_4-9p-encounter-v2.0/dataset.html and http://pdssbn.astro.umd.edu/holdings/dif-c-hriv-3_4-9p-encounter-v2.0/dataset.html

comet. For the later images, it can decrease significantly with time (Fig. 1), and this is taken into account in the analyses. Phase angle (Sun-Target-Spacecraft) varied from 62.9° to 71.6° during 800 s. Such variation and photometric errors (Klaasen et al., 2008, Li et al., 2007) do not influence on conclusions of our paper and were not considered, but they may be included in our future models. For considered images, errors of absolute calibration were less than 5% and errors of calculation of relative brightness were even smaller (Klaasen et al., 2008). Discussion of how to avoid some specific problems with calculation of peak brightness is presented in Section 2.3.

[Table 2]

[Figure 1]

We consider here only images taken through a clear filter. For all images we use the mid-time of the exposure, an important point for the earliest images where the time from impact is noticeably different at the start and end of the exposure (note that some authors have used the start of the exposure time interval). Times are all measured from the time of impact, i.e. the image in which the first sign of an impact occurs. This relative time is much better known than the absolute time (which is uncertain by about 2 seconds) but is still limited by not knowing when the impact occurred within the image that first shows the impact, i.e. an uncertainty of about 50 msec full range. As in other DI papers, original images were rotated by 90° in anti-clockwise direction.

2.2. Calculation of relative brightness

In DI images, calibrated physical surface brightness (hereafter CPSB, always in $\text{W m}^{-2} \text{sterad}^{-1} \text{micron}^{-1}$) is presented. Below sometimes we designate it simply as brightness. For series *Ma*, *Ha*, and *Hc* (see Table 2), we considered the differences in brightness between images made after the impact and a corresponding image made just before the impact (at $t=-0.057$ s for MRI images and at $t=-0.629$ s for HRI images) in order to eliminate the difference between the brightness of the nucleus and the coma. For other series we considered current images.

The relative brightness Br of the brightest pixel in an image is presented in Fig. 2 for different times. It is considered that $Br=1$ at $t=4$ s. Overlapping of considered time intervals for different series of images allowed us to calculate the relative brightness at different times, though due to not ideal calibration the values of peak brightness at almost the same time could be different for different series of images. For example, typical values of the peak brightness in series *Hb* are greater by a factor of 1.6 than those in series *Mb*. For calculations of Br for images consisted of 1024×1024 pixels, we did not consider pixels which had coordinates x or y equal to 512 or 513 (for numeration beginning from 1) because such pixels on RADREV images could be by a factor of 1.1-1.2 brighter than other close pixels and even than the brightest pixel among all pixels exclusive for pixels with the above coordinates. The brighter pixels at x and y equal to 512 or 513 cannot be detected as too bright pixels with the use of quality and bad pixel maps, as they look like as neighboring pixels in these maps. If we did not exclude pixels with such coordinates, then the brightest pixel often was located on the border of two quadrants (each quadrant consists of 512×512 pixels). For series *Hc* we did not exclude pixels constituting a brighter line at $x \approx 256$. CPSB of the brightest pixel at $t \sim 4-800$ s was greater than a typical CPSB of the comet nucleus before the impact by a factor of $\sim 5-6$. The brightest pixel corresponded to smaller projected area of the ejecta at closer spacecraft-comet distance. It could cause greater fluctuations of Br at greater t . The

observed square region corresponding to one MRI pixel is greater by a factor of 25 than that corresponding to one HRI pixel. Therefore, fluctuations of Br for HRI images could be greater than those for MRI images.

[Figure 2]

2.3. Saturated and ‘hot’ pixels and cosmic ray signatures

In this subsection we discuss some factors that could spoil some DI images in such a way that they may not truly represent a real picture, and the brightest pixel on some image may not correspond to the brightest point of the DI cloud. Discussions presented in our paper are based on analysis of RADREV images in supposition that such images give true information about the peak brightness. However, in some DN (uncalibrated) images, there were large regions of saturated pixels, which may not allow one to calculate accurately the peak brightness. The official minimum value of a digital number (DN) to define a saturated pixel equals 10,000. There were no saturated pixels in series Ma and Ha , exclusive for small regions at $t \leq 2$ s for MRI images and at $t \approx 1$ s for HRI images. The linear size of the region with $DN > 10,000$ was greater than that of the region inside the closest contour ($CPSB = 1.75$ for series Mb and $CPSB = 3$ for other series) considered in Section 5 usually by a factor of 1.4-1.5, 1.5-1.7, and 1.9 for series Mb , Hb , and Hc , respectively. In the case of a large region with $DN > 10,000$, one cannot be sure that the coordinates of the brightest pixel and the value of Br for a DI image represent correctly the brightest spot of the cloud. Therefore, the actual values of the peak brightness and the location of the brightest pixel at $t > 100$ s can differ from the values based on analysis of RADREV images.

At $t \geq 665$ s coordinates of the brightest pixel were the same for a group of HRI images, but were different for different groups of images. The values of DN for the pixel of some group that is the brightest pixel for another group were usually greater by > 1000 than those for nearby pixels (for all such pixels $DN > 10,000$), i.e. some saturated pixels were ‘hot’. At $737 \leq t \leq 802$ s for series Mb or at $665 \leq t \leq 772$ s for series He , coordinates of the brightest pixel were exactly the same for several images. It can mean that some pixels became ‘hot’ when the distance R between the spacecraft and the nucleus became small and the brightness in DN increased for corresponding DN (uncalibrated) images. Therefore, the increase of Br at these time intervals could be caused not only by the increase of peak brightness of the cloud, but also by behavior of ‘hot’ pixels at small R .

The brightness of the pixel that was the brightest pixel at $EXPID = 9000990$ (and differed by more than 3000 DN from that for close pixels) did not differ much from that for close pixels if we consider other DN HRI images. Therefore we suppose that the brightest pixel at $EXPID = 9000990$ belonged to a small signature of a cosmic ray, and the jump in Br up to 1.4 at $t = 529$ s in Fig. 2a was caused by the signature. The pixel corresponding to this maximum was not detected belonging to a signature of a cosmic ray when we used codes for removal of cosmic ray signatures considered by Ipatov et al. (2007). The expected number of signatures of cosmic rays in an image consisted of 1024×1024 pixels is about 8-16 at $INTIME = 1$ s (Ipatov et al., 2007) and about 5-10 at $INTIME = 0.6$ s (the latter value of $INTIME$ is for images from series Hb). A pixel of a cosmic ray signature can be the brightest pixel if it is located in the region corresponding to the bright part of the cloud of ejected material. The size of such region in pixels (and so the probability that a cosmic ray signature corresponds to the peak brightness) is greater for smaller R and for HRI images than for MRI images.

2.4. Time variation of peak brightness

The decrease of the relative peak brightness Br at $1 < t < 8$ s (Fig. 2) was caused mainly by the decrease of temperature of ejected material. Exclusive for the first three seconds (when the maximum brightness varied considerably), the temperature did not vary considerably. At $3 < t < 700$ s most of the values of Br were in the range of 0.95-1.06. Such relatively constant values might be caused by that the optical thickness of the corresponding pixel mainly exceeded 1.

At $t \sim 100$ -800 s, and especially at $t \sim 650$ -800 s, one can see a tendency to increase of Br with t (Fig. 2). This relatively small increase of Br , the increase of Br at $10 < t < 30$ s, and some local maxima of Br (equal to 1.056, 1.08, 1.08, and 1.2 at $t=30$, 92, 385, and 665 s, respectively) could be caused by the increase of reflectance of ejected material. The increase of reflectance could be associated with a small increase of the number of small icy particles due to destruction of larger particles in the cloud or/and due to the increase of the fraction of icy particles among new ejected material. The latter increase could be associated with the increase of fraction of ice with depth and/or with conglomerates of ice in the crater. Small increase of Br at $10 < t < 30$ s could be also caused by the increase of both the number and fraction of icy particles due to the outburst that mainly began at 10 s (see Section 6.2). As regions inside the contours $CPSB=3$ mainly increased at $t > 100$ s, the amount of observed material on a line of sight through central parts of such regions could also increase, and it could cause the increase of peak brightness (if the peak optical thickness was less than 1).

2.5. Position of the brightest pixel

Time variations of the position of the brightest pixel in a considered image relative to the position of the brightest pixel in MRI images at $t=0.001$ s and $t=0.06$ s are presented in Fig. 3a. The latter position is denoted as the place “I” of impact. The point “E” corresponding to the place of main ejection (the brightest pixel at $t=0.165$ s for series *Ma*) is located 1 MRI pixel (5 HRI pixels) below the point “I”. These places were discussed by Ernst et al. (2006) and Ernst and Schultz (2007). In Fig. 3 we consider the differences in brightness between a current image from series *Ma* (or *Ha*, or *Hc*) and an image before impact. The position of the brightest pixel is also presented in Figs. 4-8. Usually coordinates of the brightest pixel for a subtracted image are the same as those for a corresponding original image, but they could be different for some images (e.g., for the image of series *Ma* at $t=0.282$ s).

The x -shift of the brightest pixel from the points “I” and “E” was mainly about 5-15 HRI pixels at $t \sim 0.2$ –12 s and about 20-26 HRI pixels at $t \sim 13$ –36 s. Y -coordinate of the brightest pixel mainly decreased (and the absolute value of y -shift increased as $y < 0$) with time at $t < 3$ s, was approximately the same at $t \sim 4$ -12 s, but at a greater t it became closer to 0. At $t=3.3$ s the y -shift equaled to 8 MRI pixels (which correspond to 40 HRI pixels and 700 m), i.e. the mean velocity of the brightest pixel was a little more than 200 m s^{-1} .

[Figure 3]

The angle ϕ of the direction from the brightest pixel at $t=0.215$ s (i.e., from the place “E” of ejection) to the brightest pixel at a current time is presented in Fig. 3b for HRI images from series *Ha* and *Hc*. This direction corresponds to the main direction of ejection of the brightest material. For x -axis, $\phi=0$. As it is seen from Figs. 5-6 in (Schultz et al., 2007), the angle ϕ_i characterizing the direction of the impact was about -60° , and the angle of direction to the downrange plume was about -70° at $t \sim 0.3$ -0.6 s. During the

first 12 s, $\varphi < \varphi_i$ (Fig. 3b). There was a jump of x and y coordinates of the brightest pixel at $12 < t < 13$ s. Just after the above jump, there was a small increase of Br (see Fig. 2). About 2-5 s could be needed for material to pass ~ 500 m from the place of ejection to the brightest place of the cloud observed at $t \sim 5-35$ s. The jump can be associated with a change of the direction of main ejection at $t_e \sim 10$ s by about 50° to the left. At $13 < t < 60$ s the angle φ was mainly smaller (and closer to φ_i) for greater t .

2.6. Contours of fixed brightness considered

In our opinion, the studies of contours of $CPSB = \text{const}$ give more information about the amount of ejected material per unit of time than analysis of Br . DI images were calibrated in such a way that brightness of comet's surface outside the region of the cloud of ejected material did not differ with distance R between the cameras and the nucleus. Therefore, we compare the sizes of regions inside contours in kilometers.

In Figs. 4-6 we consider contours corresponding to $CPSB = \text{const}$ for the differences in brightness between Ma or Ha images and a corresponding image (from the same series) made before impact. In contrast to the above figures, in Figs. 7-8 we consider $CPSB$ contours for images (for series Hb and Mb), but not for their differences in brightness with another image made before impact. Maximum values of $CPSB$ are about 4.5-4.8 for series Ha and exceeded 4.2 (exceeded 4.7 at $t \leq 3.3$ s) for series Ma . For series Mb , the maximum values are about 2. Therefore, the values of $CPSB$ for contours presented in Fig. 8 (series Mb) are different from those in Figs. 5-7 (series Ha and Hb).

[Figure 4, Figure 5, Figure 6, Figure 7, Figure 8]

2.7. Optically thick regions

The brightness in an image depends not only on thickness of a dust cloud, but also on reflectance and temperature of material. For most images from series Ma and Ha , maximum values of $CPSB$ are greater than 3 by a factor of >1.5 . We do not think that for $t > 1$ s the temperature could vary such considerably inside the region at $CPSB > 3$. As the brightness of optically thick region is almost the same for different parts of the region, only part of a region inside the contour $CPSB = 3$ could be optically thick. In Figs. 4-6, the maximum distance of this contour from the place of ejection was less than 1.5 km and usually did not exceed 1.3 km. It means that the size of the region of essential opaque probably did not exceed 1 km. Our studies do not contradict to the results by Harker et al. (2007), who concluded that the optical depth is less than unity for all the times considered by the ground-based IR observations, but our results do not agree with the theoretical models by Holsapple and Housen (2007), who predicted a central opaque region of constant brightness extending to about 5 km height above the comet for the first 1.5 h.

2.8. Differences in velocities of particles and contours of fixed brightness

Actual velocities of particles can be greater than the velocities of the contours $CPSB = \text{const}$ for several reasons: (1) we see only a projection of velocity onto the plane perpendicular to a line of sight; the real velocity can be greater than the projected velocity by a factor of 1.5-2. Richardson et al. (2007) suppose that the ejecta are likely nearly in the plane of the sky and that the de-projection factor is about 2; in principle, much larger factors than 2 are also possible; (2) if the same amount of material moves from distance D_1 from the place of ejection to a greater distance D_2 , then the number of particles on a line of sight (and so the brightness) decreases (at $R \gg D$) by a factor of D_2/D_1 (the farther is ejected material from the crater, the smaller is a spatial density, and for an abstract model of continuous ejection with a fixed velocity and fixed production of dust, the

brightness is proportional to D^{-1}); (3) ejected particles become cooler with time and so they become less bright. On the other hand, the light from the impact illuminated the dust which was near the comet before the impact. The velocities considered in the present paper likely correspond mainly to small icy particles (see Sections 1.3-1.4), and typical velocities of large particles were smaller than these velocities.

3. Ejection of material observed during the three seconds after impact

In this section we study velocities, temperatures, and rates of ejection of material observed during the first three seconds after impact. Only MRI images from series *Ma* are analyzed. For such images, the distance R from the DI cameras to the place of impact, and, thus, the image scale, can be considered to be approximately constant. For all images considered in Section 3 and in Figs. 4 and 9, we study the difference in brightness between a current image and the image made at $t=-0.057$ s.

3.1. Velocities of material observed during the first second

Images from series *Ma* consisted of 64×64 pixels, but only 32×32 pixels are presented in Fig. 9 (in Figs. 4-8 all pixels described in Table 2 are presented). In Fig. 9a white region corresponds to $\text{CPSB} \geq 3$, and in Fig. 9b it corresponds to $\text{CPSB} \geq 0.5$, but both sub-figures present the same images. CPSB of the brightest pixel in an image has peaks at $t \sim 0.22-0.28$ s ($\text{CPSB}=9.7$) and at $t \sim 0.52-0.64$ s ($\text{CPSB}=9.5$). The peaks correspond to the increase of temperature and amount of material ejected per unit of time. Note that the two images at 0.22 and 0.28 s are both saturated at the brightest pixel, so its real brightness can be greater.

[Figure 9]

3.1.1. Velocities of hot material

At $t=0.34$ s the peak brightness in Fig. 2 was smaller by a factor of 1.6 (or more if saturation is taken into account) than at $t=0.28$ and $t=0.22$ s. One possible explanation of the decrease in the maximum brightness is that a considerable fraction of the brightness at $t \sim 0.22-0.28$ s was due to the light from the hot place of impact. More likely, the ejecta were very hot and cooled rapidly.

In images at $t=0.34$ s and $t=0.4$ s, there are two spots of ejected material corresponding to two different ejections. The material which formed the brightest pixel of the lower spot at $t=0.34$ s was located about 8 pixels (i.e., 0.7 km) below the brightest pixel at $0.165 \leq t \leq 0.224$ s. The velocity of this material exceeded $0.7/(0.34-0.165) \approx 4$ km s^{-1} . At $t=0.165$ s the bright spot was small and had a center at the point “E” (the point is discussed in Section 2.5), so most of material which formed the lower spot in Fig. 9 at $t=0.34$ s could have been ejected after $t=0.165$ s. The lower part of the contour $\text{CPSB}=3$ of the lower spot was located 10, 7 and 2 pixels below the point “E” at $t=0.34$, 0.282, and $t=0.224$ s, respectively. The difference in 5 pixels (435 m) for the latter two times corresponds to the projection v_p of velocity onto the plane perpendicular to the line of sight equal to $0.435/0.058 = 7.5$ km s^{-1} and to the beginning of the main ejection of the material of the contour at $t_e=0.2$ s. A real velocity v (not a projection) of material could exceed 10 km s^{-1} . This velocity was mentioned earlier by several other authors, e.g., by A’Hearn et al. (2005). In the absence of an internal source of energy (cf. Holsapple and Housen, 2007), conservation of energy limits the mass with $v > 10$ km s^{-1} to less than the mass of the impactor. Holsapple and Housen (2007) argue that the high velocities at the beginning must be due to extra acceleration.

In the image made at $t=0.4$ s, the lower spot is by a factor of 3 less bright than that

at $t \leq 0.34$ s. It shows that the brightness of material forming the lower spot decreased with time. The flash which caused the lower spot can be associated with vaporization of the impactor and part of the comet. The second flash which caused the upper spot may be associated with the first eruption of material at the surface. Schultz et al. (2007) considered that the initial downrange plume is likely derived from the upper surface layer (\sim projectile diameter), and A'Hearn et al. (2008) concluded that the bulk of H_2O ice is well within 1 m, and probably within 10 cm, of the surface.

3.1.2. Velocities of cooler material

The brightness of the brightest pixel in an image increased monotonically at $0.34 \leq t \leq 0.58$ s, and the vertical size of a region with $\text{CPSB} > 3$ increased from 4 to 13 pixels (from 350 to 1130 m) at $0.34 \leq t \leq 0.82$ s. Therefore, there was a considerable continuous ejection of material at time of ejection $0.34 \leq t_e \leq 0.58$ s. If we consider the motion of the contour $\text{CPSB}=3$ for the lower edge of the upper spot at t between 0.34 and 0.46 s, then for this bright material we obtain $v_p = 1.5 \text{ km s}^{-1}$ (this is an approximate estimate, as coordinates of $\text{CPSB}=3$ at these times differed by only 3 pixels). These values of v_p are smaller than those obtained for the first ejection. Supposing that the second ejection began mainly at $t_e \sim 0.24\text{--}0.28$ s (below we use mainly **0.26 s**), we obtain that material which had $\text{CPSB}=1$ at $t=0.46$ s moved with $v_p \approx 3 \text{ km s}^{-1}$ (twice faster than the material corresponding to $\text{CPSB}=3$ at $t=0.46$ s). If moving with the same velocity, at $t=0.58$ s this material would be located at a distance D from the impact by a factor of $5/3$ (for $t_e=0.28$ s) greater than at $t=0.46$ s and would have $\text{CPSB}=0.6$ for the abstract model when brightness decreases as D^{-1} . At the estimated distance we have $\text{CPSB}=0.5$. Such difference (0.6 instead of 0.5) can be caused by a rough model (actual ejection was continuous) and by a decrease of brightness of a particle with time after the ejection (with a decrease of its temperature). All the above estimates show that some material ejected at $t_e < 0.5$ s had velocities of about several km s^{-1} .

3.2. Material ejected with velocity greater than 1 km s^{-1}

The contour $\text{CPSB}=0.1$ in Fig. 4 moved with $v_p \sim 1 \text{ km s}^{-1}$ during $1 \leq t \leq 3$ s (each time the contour corresponded to parts of the cloud consisted of different particles, most of which moved with a greater velocity than the contour). Therefore, real typical velocities of particles at such distances probably exceeded 1.5 km s^{-1} and could be $\sim 2 \text{ km s}^{-1}$. Part of such high-velocity material could be ejected during the first second. Ground-based observations made a few hours after the impact did not show a considerable amount of material ejected at such velocities. The maximum velocities of the outer part of the cloud observed from the ground were about 600 m s^{-1} . It shows that the total mass of material with $v_p > 1 \text{ km s}^{-1}$ was small compared to the mass of all ejected material. In our model considered in Sections 5 and 6.1, the fraction of material with such velocities was 0.2% (for $\alpha \sim 0.71\text{--}0.75$). Some of high-velocity particles had evaporated by the time Earth-based observers saw the cloud.

4. Estimates of velocities of ejected material based on DI images made during 800 s

In this section we estimate projections v_p of velocities of ejection at several moments t_e of ejection. Such pairs of v_p and t_e are marked below in bold and are used in Section 5 for construction of our model of ejection. Most of our estimates of the pairs of v_p and t_e were based on analysis of plots $L(t)$ in Fig. 10. For series *Ma*, we considered $L=L_y=L_i$ to be equal to the distance from the place of ejection to the contour $\text{CPSB}=\text{const}$ down in y -direction. For other series, in this figure we present the difference $L=2L_x=2L_i$

between maximum and minimum values of x for the contour. L_i characterizes the distance from the place of ejection to the contour (in x or y directions). We considered the model for which material corresponding to some local minimum (or maximum) of $L(t)$ is the same for different contours considered at different times corresponding to this minimum (or maximum). Actually any region of a dust cloud could contain particles ejected with different velocities at different times, but the above model allows one to make some estimates of characteristic velocities v_{pc} . Based on the values of L_i (L_1 and L_2) for two contours at the times (t_1 and t_2) corresponding to such local minimum (or maximum), we estimated $v_{pc}=(L_2-L_1)/(t_2-t_1)$ and $t_e=t_1-L_1/v_{pc}$. The obtained pairs of $v_p=v_{pc}$ and t_e are summarized in Table 3, and more detailed estimates are presented below.

[Figure 10]

[Table 3]

First we analyze plots corresponding to the contours CPSB=3 and CPSB=1. For the contour CPSB=1 and series *Hc*, the second local maximum of $L=2L_x=7.34$ km was at $t=56$ s. It is not clear what time it is better to choose for the time corresponding to the maximum of L for the curve CPSB=3 at series *Ha* and *Hc* in Fig. 10, as the values of L are almost the same ($L\approx 2$ km) at $t\sim 16-47$ s (see also Fig. 6c). Let us suppose that particles constituting the contour CPSB=3 at $t=31$ s (this is the middle of the interval 16-46) and the contour CPSB=1 at $t=56$ s are the same. Considering that $2.6=(7.3-2.1)/2$ km were passed in $25=56-31$ s, we obtain $v_p\approx 105 \text{ m s}^{-1}$ and $t_e\approx 21=31-10$ s ($1050/105=10$). For y -direction, we have $L=L_y\approx 1.56$ km for CPSB=3 at $t=30$ s and $L_y\approx 4$ km for CPSB=1 at $t=56$ s; these data correspond to $v_p\approx 100 \text{ m s}^{-1}$ and $t_e\approx 15$ s. Larger velocities can also fit the above observations. If we consider that the particles constituting the contour CPSB=3 at $t=46$ s are the same as those constituting the contour CPSB=1 at $t=56$ s, then for y -direction we obtain $v_p\approx 240 \text{ m s}^{-1}$ and $t_e\approx 40$ s. Supposing that for series *Ma* a small decrease before the first local maximum of $L=L_y$ at $t=2.74$ s for CPSB=3 corresponds to a similar decrease at $t=4.96$ s for CPSB=0.3, we obtain $v_p\approx 930 \text{ m s}^{-1}$ and $t_e\approx 1.44$ s. For series *Hb*, there is a local minimum ($L\approx 1.5$ km) for CPSB=3 at $t\sim 100-140$ s and a local minimum ($L\approx 4$ km) for CPSB=1 at $t\sim 140-200$ s. Let us suppose that particles constituting the contour CPSB=3 at $t=120$ s and the contour CPSB=1 at $t=170$ s are the same. Considering that $1.25=(4-1.5)/2$ km were passed in $50=170-120$ s, for x -direction we obtain $v_p\approx 25 \text{ m s}^{-1}$ and $t_e\approx 90=120-30$ s ($750/25\approx 30$). For y -direction at the same times, we have $v_p\approx 16 \text{ m s}^{-1}$ and $t_e\approx 73$ s.

We suppose that for series *Hb*, particles constituting the contour CPSB=0.3 at $t=100.4$ s are the same as those of the contour CPSB=1 for series *Hc* at $t=55.6$ s. Considering that $4.3=(15.9-7.3)/2$ km were passed in 45 s, for x -direction we obtain $v_p\approx 95 \text{ m s}^{-1}$ and $t_e\approx 10$ s. For y -direction, we got $v_p\approx 105 \text{ m s}^{-1}$ and $t_e\approx 17$ s. These estimates can be more accurate than corresponding estimates for CPSB=1 and CPSB=3, as the peak of CPSB=0.3 in Fig. 10 is more sharp than that for CPSB=3.

For series *Mb* and the contour CPSB=0.3, the increase of L ($L\approx 12$ km) began at $t\sim 410$ s. For series *Hb* and the contour CPSB=3, the growth of L ($L\approx 1.5$ km) started at $t\sim 140$ s. Let us suppose that particles constituting the contour CPSB=3 at $t=140$ s and the contour CPSB=0.3 at $t=410$ s are the same. Considering that $5.25=(12-1.5)/2$ km were passed in $270=410-140$ s, for x -direction we obtain $v_{px}\approx 20 \text{ m s}^{-1}$ and $t_e\approx 100\approx 140-38$ s ($750/20\approx 38$). For y -direction for the same times, we obtain $v_{py}\approx 26 \text{ m s}^{-1}$ and $t_e\approx 115$ s. The above estimates of v_p are very approximate, but they clearly show that the values of v_p at

$t_e \approx 70-115$ s are smaller by a factor of several than at $t_e \approx 15-35$ s.

Estimates presented below are based on other approaches. We consider the model of motion of material started from the contour CPSB=3 at $t=8$ s with $v_p=240$ m s⁻¹ and moved down along the y -axis (if the material moved all the time with such velocity, then it was ejected at $t_e=4.4$ s). At $t=12.25$ s its distance D from the place of impact is greater by a factor of 2.18 than at $t=8$ s ($D=875$ m at $t=8$ s, and about 1030 m are passed during the next 4.25 [=12.25-8] s), and its brightness should decrease by this factor (i.e., from 3 to 1.38). At the place in the image at $t=12.25$ s where the material should come with $v_p=240$ m s⁻¹, CPSB is ~ 1.36 , which is close to the expected value of 1.38. For other considered values of v_p , the difference in CPSB was greater.

The lower part of the contour CPSB=0.03 in Fig. 8b (at $t=139$ s) was located about 22.5 km from the place of ejection. All particles of this part of the contour had velocities $v_{py} > 160$ m s⁻¹. For x -direction and the same contour, $L=47$ km and $v_{px} > L/2t = L_x/t \approx 170$ m s⁻¹. As there was also material outside of the contour CPSB=0.03, there could be many particles with $v_p \sim 200$ m s⁻¹. The values of $v_p \sim 100-200$ m s⁻¹ are in accordance with the ground-based observations of velocities presented in Table 1.

5. Models for calculation of time variation of rate of ejection

In Section 5 we describe our models for calculation of velocities and rates of ejection. Such models were not considered in our previous studies (Ipatov and A'Hearn, 2008a). In our estimates of relative rates r_{te} of ejection at different times t_e of ejection or with different projections v_{model} of velocity of ejection, we used sizes of the bright regions in DI images made at times t and obtained relationships between t and t_e , and we supposed that typical projection $v_p = v_{\text{expt}}$ of velocity of the edge of a bright region is proportional to t^α . The values of α for which the dependence of v_{model} on t_e corresponding to $v_{\text{expt}}(t)$ better fits the data presented in Table 3 are about 0.71-0.75 (see details of our studies below). If it is not mentioned specially, we use such values of α in our paper.

For theoretical models, Housen et al. (1983) and Richardson et al. (2007) obtained that ejection velocity v is proportional to $t_e^{-\alpha}$, where α is between 0.6 (the theoretical lower limit corresponding to basalt) and 0.75 (the theoretical upper limit). They considered that the cratering event is primarily governed by the impactor's kinetic energy at $\alpha=0.6$ and by momentum at $\alpha=0.75$. According to Holsapple (1993), $\alpha=0.71$ for sand and dry soil and $\alpha=0.644$ for water, wet soil, and soft rock. The designations (e.g., α) in the above papers were different from those in our paper. The exponents of the time dependences of the relative volume f_{et} of observed material ejected before time t_e and the relative rate r_{te} of ejection, and the exponents of the velocity dependence of the relative volume f_{ev} of material ejected with velocities greater than v are presented in Table 4 for the above four values of α . These exponents were obtained based on Table 1 of the paper by Housen et al. (1983).

[Table 4]

In Fig. 11 we present the plots of $v_{\text{expt}} = v_p = c \times (t/0.26)^{-\alpha}$ for 4 pairs of α and c . The values of $v_{y\text{min}} = L_y^*/(t-0.26)$ ($v_{y\text{min}} = L_y^*/t$ at $t < 0.3$ s) and $v_{x\text{min}} = L_x^*/(t-0.26)$ show the minimum velocities (in km s⁻¹) needed to reach the edge of the bright region in a DI image considered at time t from the place of ejection for the motion in y -direction (for series Ma) or in x -direction (for other series), respectively. As noted in Section 3.2, we suppose that the second ejection began mainly at $t_e \approx 0.26$ s. We considered that $L_y^* = 0.95 \times L_r$ and $L_x^* = 0.5 \times 1.076 \times L_r$, (the values of L_y^* and L_x^* are in km), where the

relative linear size L_r of the bright region was calculated based on the values of L presented in Fig. 10 for the contour CPSB=1.75 for series *Mb* and the contour CPSB=3 for other series. It was considered that $L_r=1$ at $t=1$ s. For contours CPSB=3 at $t=1$ s, we have $L=L_y=L_y^*=0.95$ km for series *Ma* and $L=2L_x=2L_x^*=1.076$ km for series *Ha*. The ratio L_x/L_y varied with time.

[Figure 11, Figure 12]

The values of L in km at approximately the same time can be different for different series of images considered. Therefore we cannot simply compare L for different images, but need to calculate L_r , which compensates non-ideal calibration of images and characterizes the size of the bright region. Starting from series *Ma* and *Ha*, we compared the values of L at approximately the same time for two series, considering L_r to be the same at the same time for different series. For the second series considered in such comparison, we calculated the ratio L_r/L at this time and then the values of L_r for other times. Considering that the time needed for particles to travel distance L_x^* in x -direction is equal to $dt=1.076L_r/(2v_{\text{expt}})$, we find the time $t_e=t-dt$ of ejection of material of the contour of the bright region considered at time t . Using the obtained relationship between t and t_e (Fig. 12) and considering that $v_{\text{model}}(t_e)=v_{\text{expt}}(t)=c \times (t/0.26)^{-\alpha}$, in Fig. 11 we present plots of v_{model} vs. t_e for four pairs of α and c . Actually we analyzed plots $v_{\text{model}}(t_e)$ for a greater number of pairs (α and c) trying to find the plots that better fit the pairs of v_p and t_e presented in Table 3 (the values of v_p are marked as vy_{obs} and vx_{obs} in Fig. 11). Note that velocity distributions over t and t_e were different.

Based on the values of L_r , we calculated (see Fig. 13) the values $V_r=L_r^3$ of the relative volume of material inside the bright region discussed above and the relative rate $r_{te}=L_r^3 \times t^{-\alpha}$ of ejection (which is proportional to $V_r \times v_{\text{expt}}(t)$) for $\alpha=0.6$, $\alpha=0.644$, $\alpha=0.71$, and $\alpha=0.75$. The less is the velocity, the more particles are in the bright region, and the less rate of ejection is needed to form the same bright region. Based on these dependences of r_{te} on time t and on the obtained relationship between t and t_e , we constructed the plots of dependences of r_{te} on t_e (see Fig. 14). These rates were used for construction of plots of the relative volume of ejecta launched before t_e vs. t_e (Fig. 15) and of the relative volume of ejecta with velocity $v_p > v_{\text{model}}$ vs. v_{model} (Fig. 16). While constructing Figs. 15-16, we considered only material ejected before t_e that corresponds to the last value of time $t=803$ s at which we analyzed the edge of the bright region.

[Figure 13, Figure 14, Figure 15, Figure 16]

6. Time variations of rates and velocities of ejection obtained in our models

6.1. Time variation of ejection rate

The relative volume V_r of the considered bright region has local maxima at $t \sim 2-4$ s and $t \sim 20$ s (Fig. 13). The volume (and the size of the region CPSB ≤ 0.3 for series *Mb* in Fig. 10) increased with time at $t \sim 100-800$ s and especially at $t > 7$ min. This increase is in accordance with the increase of the brightening rate obtained at the ground-based observations discussed at the beginning of Section 1.4.

The maximum of the rate r_{te} of ejection for $\alpha=0.71$ and $\alpha=0.75$ and local maximum of r_{te} for $\alpha=0.6$ and $\alpha=0.644$ were at $0.57 \leq t_e \leq 0.69$ s. These times correspond to the end of the interval of the maximum brightness ($Br \geq 2$ at $0.46 \leq t \leq 0.76$ s and $Br=2.14$ at $0.52 \leq t \leq 0.64$ s). A little smaller values of the times for $Br=2.14$, compared to the times for the rates, could be caused by larger temperatures at smaller t (i.e. by non-linear dependence of Br on ejection rate). The maximum of the rate obtained at $t_e < 0.1$ s and

$\alpha < 0.65$ shows that the model with such α is not correct for such small t_e .

For most suitable pairs of α and c , we obtained the local maximum of relative rate r_{te} at $t_e = t_{elm} \sim 9-11$ s (see Table 5). At this time there was a jump of the direction from the place of ejection to the brightest pixel (see Section 2.5). Typical projections v_p of ejection velocities at $t_e \sim 10$ s were $\sim 100-200$ m s⁻¹ (see Fig. 11). The local peak of the rate of ejection at $t_e \sim 10$ s explains the velocities of observations presented in Table 1.

[Table 5]

Smaller values of peak brightness observed at some time intervals (e.g., at $100 < t < 200$ s) could be caused by that sublimation converts bright ice to gas that does not show up in the white light images and by that the fraction of small ejected particles decrease with time. Therefore, at some time intervals the rate of ejection could be higher than the rate r_{te} based on size of the bright region. On the other hand, destruction of large particles could produce smaller particles.

6.2. Triggered outburst

In our model, the rate r_{te} of ejection increased on two intervals and decreased on two intervals of t_e (Fig. 14), while theoretical dependence of r_{te} on t_e is always monotonic with exponents presented in Table 4. At $t_e \sim 0.3-0.8$ s, r_{te} can be partly approximated by $r_{te} = c_r \times (t_e - c_t)^{0.2}$, where c_r and c_t are some constants. The exponent 0.2 corresponds to $\alpha = 0.6$. The observed ejection at $1 < t_e < 60$ s differed from theoretical dependences (Fig. 14) and could be partly caused (especially at $t_e \sim 10$ s, when there was a local maximum of ejection rate) by a considerable outburst initiated by the impact (the outburst was suggested in our abstracts: Ipatov and A'Hearn, 2008b, 2009). At $t_e \sim 60$ s there was a sharp (by a factor of about 3) decrease of the ejection rate r_{te} (Fig. 14b) and a sharp change of the direction from the place of ejection to the brightest pixel (Fig. 3b). It could be caused by a sharp decrease of the outburst. The dependence of r_{te} on t_e was proportional to $t_e^{-0.25}$ at $t_e \sim 70-500$ s (the exponent -0.25 corresponds to $\alpha = 0.75$). For $\alpha = 0.71$ and $\alpha = 0.75$, the values of r_{te} at $t_e \sim 550-650$ s were greater by a factor of 1.4-1.5 than those at $t_e \sim 400$ s (Fig. 14b), though $t_e^{-0.25}$ and $t_e^{-0.13}$ (corresponding in Table 4 to $\alpha = 0.75$ and $\alpha = 0.71$) decrease with t_e . The difference could be caused by the increase of the outburst, or/and by material falling back on the comet, or/and by the change of composition (to more icy) of ejected material, or/and by destruction of larger particles. As r_{te} can be considered to be approximately proportional to $t_e^{0.2}$ at $t_e < 0.7$ s and to $t_e^{-0.25}$ at $t_e \sim 70-500$ s, we can conclude (using also data from Table 4) that the material of the comet ejected at $t_e < 0.7$ s could be more solid than that at $t_e > 1$ s, and especially at $t_e > 70$ s.

In our model, about a half of observed material was ejected during the first 100-150 s (Fig. 15 and Table 5). Theoretical curves of the relative volume f_{et} of material ejected before t_e vs. t_e at $t_e > 100$ s increased sharper than our obtained curves. Such difference can be caused by that the mean sizes of ejected particles increased with time, but mainly small particles were observed and considered in our model. In Section 8.2 we discuss that at $t_e > 70$ s time variations of velocity of material ejected due to the outburst could be smaller than for normal cratering. In this case, the fraction of material ejected after 70 s is greater than for the model with exponential dependence of v_{model} on t_e .

6.3. Amounts of material ejected with different velocities and at different sizes

Theoretical and our model curves of the relative volume f_{ev} of material ejected with velocity greater than $v = v_{\text{model}}$ vs. v are presented in Fig. 16. Besides theoretical exponents from Table 4, in this figure we consider also proportionality to $v^{-2.25}$ obtained

in experiments (Gault et al., 1963; Petit and Farinella, 1993; Holsapple and Housen, 2007). Comparison of the curves shows that the fraction of observed particles with $30 < v_p < 800 \text{ m s}^{-1}$ was greater than for all theoretical models, with a maximum difference at $v_p \sim 30\text{-}60 \text{ m s}^{-1}$. The difference could be caused by that there could be a lot of outburst particles with $v_p \sim 30\text{-}60 \text{ m s}^{-1}$. Note that the values of f_{et} and f_{ev} are considered (see Section 5) to be equal to 1 for the material ejected before the time t_e corresponding to the bright region at $t=803 \text{ s}$.

Let us estimate the total mass M_t of observed ejected material. The mass M_1 of droplets ejected during the first second is considered to be about $4 \cdot 10^3 \text{ kg}$ (Melosh, 2006). Material ejected during the first second was less icy, but hotter than other ejected material. Therefore it is not clear whether it was brighter or not than the later ejecta. The values of the fraction f_1 of material ejected during the first second that are presented in Table 5 for six considered pairs of α and c correspond to $M_t = M_1/f_1 \sim (1\text{-}4) \cdot 10^5 \text{ kg}$, with $M_t \approx 2 \cdot 10^5 \text{ kg}$ for the most suitable pairs. The value of M_t is less than the total mass M_{tot} of all ejected particles because the minimum velocities v_{e803} considered in our models (see Table 5) are greater than the escape velocity $v_{es} = 1.7 \text{ m s}^{-1}$ by a factor of more than 4, and our estimate of M_t corresponds only to small particles that mainly contribute to the brightness of the cloud. The obtained values of M_t are in accordance with most estimates of the total mass of ejecta with $d < 3 \text{ }\mu\text{m}$ presented in Table 1. This is a confirmation of the previous conclusion (see Section 1.3) that diameters of the particles that mainly contribute to the brightness of the cloud are less than $3 \text{ }\mu\text{m}$. As $v_{\min} = v_{e803} > v_{es}$, the particles considered in our model presented in Figs. 11-16 did not fall back on the comet.

Below we compare our model results with theoretical estimates and Hubble Space Telescope (HST) observations. For $\alpha=0.71$ and $c=2.5$, the fractions of material ejected with $v_p \geq 200 \text{ m s}^{-1}$ (at $t_e \leq 6 \text{ s}$) and $v_p \geq 100 \text{ m s}^{-1}$ (at $t_e \leq 15 \text{ s}$) equaled to 0.07 and 0.17, respectively. At $M_1 = 4 \cdot 10^3 \text{ kg}$, the amount of material ejected with such velocities equaled to $1.6 \cdot 10^4 (= 4 \cdot 10^3 \cdot 0.07/0.017) \text{ kg}$ and $4 \cdot 10^4 \text{ kg}$, respectively. Note for comparison that for all models presented by Richardson et al. (2007) in their Fig. 19, the total mass of material ejected with $v > 100 \text{ m s}^{-1}$ was about 10^3 kg and was less than 1% of the total ejected mass for most values of effective strength S considered. In our models at $\alpha \sim 0.71\text{-}0.75$, about 2% of material were ejected during the first second with $v_p > 400\text{-}500 \text{ m s}^{-1}$.

At $\alpha \sim 0.71\text{-}0.75$, our model predicts ejection of 5% of observed material with $v_p \geq 280 \text{ m s}^{-1}$. This is a little greater than 3% based on the HST observations (Feldman et al., 2007). One of possible reasons of the difference is that our 5% are calculated not of all observed ejected material, but only of the material observed during 800 s.

6.4. Duration of ejection

The contours analyzed are easily explained by continuous ejection of material during at least 10 minutes after collision. For example, the values of t_e corresponded to the bright region at $t=803 \text{ s}$ exceeded 10 min for all models considered (see Table 5). Nevertheless, it is difficult to make firm conclusions about the time when ejection finished. In principle, the time of ejection could be smaller than 10 min, as variation of brightness of the cloud might not depend only on the rate of ejection and the relation between flux and ejected mass was non-linear (see Section 1.4). The bright region of the cloud, which increased at $t \sim 100\text{-}800 \text{ s}$ (see Fig.10), could be partly caused by the particles landed back on the nucleus and by slow moving particles that had been ejected a few minutes before the time t when an image was made. On the other hand, the particles

that mainly contributed to the brightness of the cloud were small, at $t < 13$ min mainly had velocities exceeding the escape velocity by at least a factor of several, and so did not fall back on the comet. Large particles that landed back on the nucleus made a small contribution to the brightness of the cloud. If ejection finished e.g. at $t_{\text{end}} \sim 6-7$ min, then all bright regions observed up to $t \sim 13$ min must be caused by particles ejected before t_{end} , and it is difficult to imagine that there was such considerable ejection of small bright particles with a wide range of velocities at the same time. The main argument in favor of ejection at $t_e \sim 10$ min is the existence of rays of excessive ejection close to the nucleus in images made up to 13 min (see Section 7).

According to Cohran et al. (2007), there could not be a considerable fragmentation of icy grains that increases the brightness of the cloud (for the same total mass of the cloud). As the total brightness of the DI cloud increased during the first 35-60 min (see Section 1.4), the Cohran's conclusion may show that duration of the triggered outburst could exceed 35 min. Long ejection is in accordance with the conclusion by Harker et al. (2007) that the best-fit velocity law necessitates a mass production rate that was sustained for duration of 45-60 min after impact.

7. Rays of ejected material

Bumps on the left and right edges of some contours $\text{CPSB} = \text{const}$ (see, e.g., Figs. 8a-c) were produced by the rays of ejected material (more material was ejected in some directions; see, e.g., Schultz et al., 2007). It is considered that the rays are caused by internal sources of energy of the comet released after the impact. The effect of an oblique impact could also play a role in the asymmetry of the cloud of ejected material (Richardson et al., 2007), but it could not give such sharp rays as the observed rays. In our opinion, the rays of ejected material could be caused mainly by the excess of ejection in some directions during the outburst.

In this and two next paragraphs, we consider the *upper-right bump*. For this bump, most of the values of the angle ψ between the upper direction and the direction to a bump measured in a clockwise direction were close to $65-70^\circ$ (e.g. in Figs. 6b,d, 7b,d, 8d-f), but $\psi \approx 60^\circ$ in Fig. 8a (at $t = 80$ s) and $\psi \approx 80^\circ$ in Fig. 7c (at $t = 140$ s). The upper-right bump was usually accompanied by the upper-upper-right bump with $\psi \approx 40-45^\circ$ in most images ($\psi \approx 50^\circ$ in Fig. 8e at $t \approx 350$ s). These two bumps usually had similar sizes and can be considered as two parts of one M-type bump. At $t = 2.7$ s the upper-right bump is seen for $\text{CPSB} = 1$, but is not seen for $\text{CPSB} \leq 0.3$. Using the obtained relationship between t and t_e for $\text{CPSB} = 3$ and taking into account that particles constituting the contour $\text{CPSB} = 1$ were ejected before those for $\text{CPSB} = 3$, we obtain that already at $t_e \approx 1$ s there could be excessive ejection in this direction. At $t \sim 5-14$ s ($t_e \sim 3-8$ s) the bump is not practically seen for the considered levels of CPSB. After $t = 15$ s the upper-right bump for $\text{CPSB} = 1$ began to increase with time. The value of $t \sim 15$ s can be correlated (a few seconds are needed for particles to reach the contour) with the changes of the direction to the brightest pixel at $t \sim 12-13$ s and $t_e \sim 10$ s (see Fig. 3) and with the beginning of a local increase of peak brightness (Fig. 2b). For the contours $\text{CPSB} = 1$, the bump is seen much better at $25 \leq t \leq 43$ s (Fig. 6d) than at $t \leq 21$ s (Fig. 6b). The most sharp bumps are seen for $\text{CPSB} = 1$ at $t = 43$ s in Fig. 6b, for $\text{CPSB} = 1.5$ at $t = 39$ s in Fig. 7a, and for $\text{CPSB} = 0.5$ at $t = 66$ s in Fig. 7b. The distance between the two last mentioned bumps is passed at velocity of ~ 120 ($= 3300 / (66 - 39)$) m s^{-1} . The ejection of material of these contours moving with such velocity was at $t_e \sim 20$ s. In Fig. 7c ($t = 142$ s) the bump of the contour $\text{CPSB} = 0.5$ is clearly seen. It is

located at distance $D \approx 4200$ m from the place of ejection. Note that D is the projection of the distance onto the plane perpendicular to the line of sight, and the real distance is larger than D . Considering that $t_e/t \approx 0.3$ (as for CPSB=0.5 and $t=66$ s), we obtain $t_e \approx 142 \cdot 0.3 \approx 43$ s and $v_p \approx 4200/(142-43) \approx 42$ m s⁻¹. Therefore, at $t_e \sim 40$ s the excess of ejection could still be considerable. It is seen from Fig. 14a that at $3 < t_e < 8$ s the rate of ejection is relatively close to the theoretical crater ejection (presented by the curve $y=0.1(x-5)^{-0.25}$), in contrast to $1 < t_e < 3$ s and $8 < t_e < 40$ s when there was a considerable outburst. Therefore the greater was the outburst, the greater were the rays of ejected material.

The upper-right bump is also seen for some outer CPSB contours at $t \sim 300-770$ s. For example, the bump of CPSB=1 is seen in Fig. 7e at $t=529$ s though the distance of the contour CPSB=1 from the place of impact is only 2 km. The contour CPSB=1 in an MRI image at $t=772$ s also has the same bump. The bumps in images made up to $t \sim 13$ min testify in favor of that there was ejection of material at $t_e \sim 10$ min. It is difficult to explain the rays close to the nucleus without the continuous outburst.

In series *Mb* at $t=139$ s for the upper-right bumps of CPSB=0.1 ($D \approx 15$ km) and CPSB=0.03 ($D \approx 25$ km), v_p exceeded 110 and 180 ($\approx 25000/139$) m s⁻¹, respectively. At $t=191.5$ s the bump of CPSB=0.03 is located at $D \approx 30.5$ km, and these values of t and D correspond to $v_p \geq 160$ m s⁻¹. These estimates show that velocities of some particles constituting the rays were $\sim 100-200$ m s⁻¹.

A small *right bump* (which became down-right with time) is seen at some contours in Figs. 5-8. For this bump, ψ increased from 90° in Figs. 5b-c (at $t \sim 4-8$ s) to 110-120° in Figs. 6d, 7d, 8f (at $t \sim 25-400$ s). At $t \sim 4-12$ s (i.e. before the jump of direction to the brightest pixel) the right bump was mainly greater than the upper-right bump, but at a greater time it was not well seen.

The “M”-type *left bump* is clearly seen for three outer contours in Fig. 8a (at $t=78$ s), for two contours (CPSB=0.1 and CPSB=0.03) in Fig. 8b ($t=139$ s), and only for the contour CPSB=0.03 in Fig. 8c ($t=191.5$ s). Therefore, considerable excessive ejection in this direction was not long (< 100 s). This bump is also seen in Figs. 6d, 7a-b (at $t \sim 25-66$ s). For the upper and lower parts of the M-bump, $\psi \approx 260^\circ$ and $\psi \approx 245^\circ$, respectively. For outer contours in Figs. 7b and 8b-c, these parts were a little smaller than the upper-right and upper-upper-right bumps. The direction from the place of ejection to the lower part of the left M-bump ($\psi \approx 245^\circ$) is opposite to the upper-right bump ($\psi \approx 70^\circ$). Both directions were approximately perpendicular to the direction of the impact. Note that one of the rays of ejected material obtained in the experiment by Schultz et al. (2007) and presented in their Fig. 31 was also perpendicular to the direction of impact. At $t_e > 100$ s instead of the left M-bump there was the *down-left M-bump*, which is less clearly seen than the left bump at smaller t_e . For two parts of the down-left M-bump, the values of ψ were about 230-235° and 210-220°. The down-left bump was still seen in images at $t \sim 400-760$ s. The above discussion shows that excessive ejection could be in different directions at different time intervals.

The *upper bump* of the outer contour is clearly seen at $t \sim 139-411$ s in Fig. 8b-f (especially, in Fig. 8c). It is also seen for the contour CPSB=1 at $t \sim 25-42$ s in Fig. 6d. The angle ψ varied from about 0 in Fig. 8b to -25° in Fig. 8f (it was -15° in Fig. 6d). The direction from the place of ejection to this bump was not far from the direction opposite to the impact direction (i.e., the bump corresponds to the excessive ejection backwards to

the impact direction), but was not exactly perpendicular to the line connecting down-left and upper-right bumps. The upper bump is not well seen in all contours in Fig. 8a (at $t=78$ s). Therefore, the upper bump of CPSB=0.03 in Fig. 8c ($t=191.5$ s) consisted mainly of particles ejected at $t_e>80$ s, and the excessive ejection backwards to the impact direction was mainly after 80 s. Schultz et al. (2007) concluded that uprange ejecta plume directed back out the initial trajectory (during the first 10 s) and at very late stage (700 s). In our studies the upper bump was more pronounced if it consisted of particles ejected at $t_e>100$ s. For experiments described by Hermalyn et al. (2008), at the middle of ejection time interval, velocities of material ejected in the uprange direction were smaller than in the downrange direction.

8. Discussion

8.1. Differences between the DI ejection and theoretical models and experiments

Conditions of ejection of material from Comet Tempel 1 were different from those for experiments and theoretical models. The great difference in projectile kinetic energy introduces challenges when scaling the laboratory results to DI conditions, e.g., some materials will vaporize that otherwise would remain in solid or liquid form (Ernst and Schultz, 2007). Mechanism of activity of Comet Tempel 1 was considered by Belton et al. (2007). Holsapple and Housen (2007) concluded that for a normal cratering mechanism only a negligible amount of mass ejected had velocities on the order of 100's of m s^{-1} and velocities of 100's of m s^{-1} that were observed are due to the particles that were accelerated by vaporization of ice in the plume and fast moving gas. The fraction of water vaporized at the impact is considered to be $\sim 0.2\%$ of the total amount of water ejected (DiSanti et al., 2007).

In Section 6.2 we discuss that the triggered outburst could increase the duration of ejection of material and the velocities of ejected material and caused the non-monotonic time variation of the rate of ejection. Below we consider a few more arguments in favor of that a considerable fraction of the observed (exclusive may be for a few first seconds after the impact) DI cloud could be produced by the outburst. Typical velocities of the leading edge of observed material ejected after the DI collision (see Table 1) were close to the velocities observed after the 2007 October 24 outburst from Comet 17P/Holmes. Montalto et al. (2008) observed a spherically symmetric dust cloud moving away from the comet nucleus with a mean projected constant velocity of 135 m s^{-1} , while the dust cloud was expanding with a mean constant velocity of 200 m s^{-1} . A spherically symmetric outer shell expanded at 430 m s^{-1} (Meng et al., 2008). The total mass of material ejected at that outburst ($\sim 1\text{-}4\%$ percents of the nucleus mass of Comet 17P, i.e. $(1\text{-}3)\times 10^{11} \text{ kg}$) was much greater than that at the DI collision.

According to Biver et al. (2007), the amount of water released at DI impact was about 0.2 day of normal activity, but that during the natural outburst on 22-23 June was about 1.4 day of normal activity (i.e., was larger than at the DI burst). At natural outburst, water was in form of gas, so the outburst was not as bright as the burst after the impact. Biver et al. (2007) concluded that it took about 4 h for water particles to sublimate. Therefore, the role of sublimation was important at $t\sim 1$ h, but it might be not considerable during the first several minutes considered in our paper.

Asteroid 7968 Elst-Pizarro, also known as Comet 133P/Elst-Pizarro, moves in an asteroidal orbit with $a=3.161 \text{ AU}$, $e=0.1644$, and $i=1.386^\circ$. The orbit of this object is stable (Ipatov and Hahn, 1997, 1999). In 1996 and 2002, this object had a cometary tail

for several months. It might be possible that cometary activity of this object was initiated by collisions with small bodies. Small inclination of the object and location of its perihelion (2.64 AU) in the center of the asteroid belt can cause a greater probability of its collisions with smaller objects, compared with the probability for a typical asteroid. The longer duration of these outbursts, compared with those from other minor bodies, could be caused by icy composition of the object Elst-Pizarro. Based on studies of the orbital evolution of Jupiter-crossing objects (Ipatov and Mather, 2003, 2004), Ipatov and Mather (2007) concluded that the object Elst-Pizarro earlier could be a Jupiter-family comet and it could circulate its orbit also due to non-gravitational forces.

A few other differences of the DI ejection from experiments are the following: Gravity on the comet (0.04 cm s^{-2}) is much smaller than that on the Earth (9.8 m s^{-2}), and masses of projectiles in experiments were small. Diameters of particles that made the main contribution to the brightness of the DI cloud are considered to be less than $3 \text{ }\mu\text{m}$, and sizes of sand particles in experiments were much larger ($\sim 100 \text{ }\mu\text{m}$). The observed DI cone of ejected material was formed mainly by small particles, which had higher velocities than larger particles.

8.2. Velocities of ejected material

Results of our studies of velocities (e.g. in Section 6.3) are in accordance with the velocity of the leading edge of the dust cloud of ejected material projected onto the plane perpendicular to the line of sight of $100\text{-}200 \text{ m s}^{-1}$, which was obtained with the use of various ground-based and space telescopes. Our estimates of projections v_p of typical velocities of ejection presented in Table 3 were about 100 m s^{-1} at $t_e \sim 10\text{-}20 \text{ s}$ and $20\text{-}25 \text{ m s}^{-1}$ at $t_e \sim 70\text{-}115 \text{ s}$. We suppose that velocities of the outburst decreased between 20 s and 70 s , but after 70 s they could stabilize. Therefore, we also considered a model *C* with $v_{\text{model}} \approx 25 \text{ m s}^{-1}$ at $t_e > 70 \text{ s}$. The volume of bright region was about the same at $t \sim 100\text{-}200 \text{ s}$, and increased at $t \sim 200\text{-}800 \text{ s}$ (Fig. 13). For the distance of the edge of the bright region from the place of ejection equal to $L = 1500 \text{ m}$ at $v_p = 25 \text{ m s}^{-1}$, we obtain $dt = t - t_e = L/v_p = 60 \text{ s}$. Therefore for the model *C*, the rate of ejection of small particles could increase at $t_e > 140 \text{ s}$ (at least until 750 s). It may be also possible that the rate at these times was about the same, but velocities decreased.

By July 8 UT (four nights after impact) the inner $\sim 15,000 \text{ km}$ were no brighter than prior to impact (Knight et al., 2007). Therefore, material with $v < 40 \text{ m s}^{-1}$ was not practically observed at that time. This low-velocity material could be sublimated (material ejected with smaller velocities was from deeper layers and could be more icy).

For all models considered by Richardson et al. (2007) and Holsapple and Housen (2007), most of the mass was ejected with $v < 3 \text{ m s}^{-1}$. For an oblique impact, on the down-range side of the ejecta plume, ejection velocities are higher and particle ejection angles are lowered compared with a vertical impact (Richardson et al., 2007). If we extrapolate a plot of v_{model} at $\alpha = 0.71$ in Fig. 11 to greater t_e , we obtain $v = 3 \text{ m s}^{-1}$ at $t_e \sim 3000 \text{ s} = 50 \text{ min}$. Probably, the ejection with $v \sim 3 \text{ m s}^{-1}$ due to normal cratering took place at smaller times t_e , together with the ejection with greater ($v_p \sim 20\text{-}100 \text{ m s}^{-1}$) velocities due to the outburst, which might continue for a long time. Besides the outburst, the differences between theoretical estimates and observed velocities are partly caused by that in the model considered by Richardson et al. (2007), all particles ejected at the same time had the same velocities and were ejected at the same distance from the place of impact. We suppose that at least at late stages of even typical crater formation, particles ejected at the same

time could have different velocities and could be ejected at different distances.

In our present model, all particles were ejected with the same velocity at each considered time. We plan to make computer simulations of the brightness of the cloud produced by particles ejected at different times with different velocities and at different ejection rates in order to choose such time variations of the rates and velocities and such velocity distributions that better fit the observations. The integration of the motion of particles will be made similar to (Ipatov and Mather, 2006). We will study the combination of models of typical crater ejection (when velocity decreases with time) and of a triggered outburst with a relatively small variations of velocity.

8.3. Formation of the Deep Impact crater

Let us compare results of DI observations with the models of crater formation considered by several authors and summarized by Richardson et al. (2007). They concluded that the DI crater formed in not more than 250-550 s (4-9 min) for the case of effective strength $S=0$ (gravity-dominated cratering). Crater formation time t_{cf} was supposed to be proportional to $S^{-1/2}$ and to be not less than 1-3 sec at $S=10$ kPa (for strength-dominated cratering). The amount of ejected material was about 2×10^7 kg at $S=0$ and about 2×10^5 kg at $S=10$ kPa. The cumulative mass of solid particles ejected at velocity greater than 10 m/s (or any other greater value) was almost the same for different models considered by Richardson et al. (2007), though the total mass of ejected material varied considerably for different values of effective strength S . Therefore, even for normal cratering, observational estimates of the total mass of fast moving small dust particles does not allow one to make reliable conclusions on the values of S . The quantity of the high-velocity ejecta increases with decreasing impact angle I (Yamamoto et al., 2005). For DI impact, $I \approx 20-35^\circ$ and the quantity must be greater than for the models of impact with $I=90^\circ$ considered by Richardson et al. (2005) and Holsapple and Housen (2007).

Observations of H_2O and OH showed (Küppers et al., 2005; Schleicher et al., 2006; Biver et al., 2007; Keller et al., 2007; A'Hearn, 2007; A'Hearn and Combi, 2007) that the amount of water exceeded 5×10^6 kg (estimates by Lisse et al. (2006) were smaller). Such estimates of water allow one to conclude that DI cratering was different from the strength-dominated cratering because the total ejected mass must be small for the latter cratering. Considering that the volume of a crater equals $V = \pi \times r_c^3 / 3$ (where r_c is radius of a crater) and density ρ is equal to 400 kg m^{-3} (Richardson et al., 2007), we obtain that $r_c = 23$ m for $\rho \times V = 5 \times 10^6$ kg (the above estimate of the minimum amount of water) and $r_c = 55$ m for $\rho \times V = 7 \times 10^7$ kg (the maximum estimate of the total mass of ejected material at $d < 2$ m presented in Table 1). Even the latter value of r_c is less than the estimate of a crater radius (75-100 m) made by Busko et al. (2007) on the basis of analysis of DI images. Schultz et al. (2007) considered a little wider range for the radius: 65-110 m. They concluded that the difference between the volume of a crater and the ejected mass is due to displaced mass for the crater. Particles ejected at the outburst probably were mainly relatively small, their contribution to the brightness could be much greater than to the total ejected mass, and most of the crater volume could be caused by typical ejection. Therefore relatively large estimates of radius of the crater by Busko et al. (2007) and Schultz et al. (2007) testify in favor of gravity-dominated cratering, and so for longer duration of typical cratering ejection, even without the outburst.

In principle, the above difference between the volume of a crater and the ejected

mass can also testify in favor of a possibility of the presence of bodies with $d > 2$ m in the ejected material, though such bodies were not observed. Diameter of the largest body definitely could not exceed 20-25 m because of the limited depth of the crater. In experiments with projectile velocity ~ 1 -10 km s⁻¹, Koschny and Grün (2001) found an upper limit for the mass of the largest ejected fragment of about 1% of the total mass. For DI at $r_c = 100$ m, such limit corresponds to $d \sim 25$ m. For porous ice-silicate mixture at exponent equal to 1.8 in mass distribution (Koschny and Grün, 2001), the increase of diameter of the largest fragment by a factor of 10 causes the increase in total ejecta mass by a factor of $10^{1.8} \approx 63$ and the increase of the radius of the crater by a factor of $63^{1/3} \approx 4$.

Holsapple and Housen (2007) obtained the time of formation of the DI crater to be about 5 min for sand-gravity scaling, 11 min for water, and much smaller for other types of soil considered (e.g., soft rocks and cohesive soil). For a typical crater ejection, duration of ejection for ≥ 10 min obtained in our studies is not in accordance with the other types of soil considered by Holsapple and Housen. As the long duration of the ejection could be due to the outburst, it is not possible to make conclusions on a type of soil.

9. Conclusions

Our studies of the projections v_p of velocities of ejected material onto the plane perpendicular to the line of sight and the relative amounts of particles ejected from Comet 9P/Tempel 1 were based on the images made by the Deep Impact cameras during the first 13 min after the impact. We considered velocities of the particles that give the main contribution to the brightness of the cloud of ejected material, i.e. mainly of particles with diameter $d < 3$ μ m.

The maximum of production of observed ejected material was at time of ejection $t_e \sim 0.6$ s. There was a local maximum of the rate at $t_e \sim 10$ s with typical projections of velocities $v_p \sim 100$ -200 m s⁻¹. At $1 < t_e < 3$ s and $8 < t_e < 40$ s the estimated rate of ejection of observed material was essentially greater than for theoretical monotonic exponential decrease. Such difference was caused by that the impact was a trigger of an outburst. There could be a sharp decrease of the outburst at $t_e \sim 60$ s. Our studies do not allow one to estimate accurately the time of the end of ejection. They do not contradict to a continuous ejection of material during at least 10 minutes after the collision. Material of the nucleus ejected during the first second could be more solid than that ejected after the first second.

Projections of velocities of most of observed material ejected at $t_e \sim 0.2$ s were about 7 km s⁻¹. As the first approximation, the time variations of characteristic velocity at $1 \text{ s} < t_e < 60 \text{ s}$ can be considered to be proportional to $t_e^{-0.75}$ or $t_e^{-0.71}$, but they could differ from this exponential dependence. The fractions of observed material ejected (at $t_e \leq 6$ s and $t_e \leq 15$ s) with $v_p \geq 200$ m s⁻¹ and $v_p \geq 100$ m s⁻¹ were estimated to be about 0.07 and 0.2, respectively, if we consider only material observed during the first 13 min. These estimates are in accordance with the previous estimates (100-200 m s⁻¹) of projection of velocity of the leading edge of the DI dust cloud based on various ground-based observations and observations made by space telescopes.

The excess ejection of material to a few directions (rays of ejected material) was considerable during the first 100 s, and it was still observed in images at $t \sim 500$ -770 s. It shows that the outburst continued after 60 s and could be at $t_e \sim 10$ min. Considerable excessive ejection began approximately at the same time $t_e \sim 10$ s when the direction from the place of ejection to the brightest pixel changed by 50°, the peak brightness began to

increase, and there was a local peak of the rate of ejection. The direction from the place of impact to the brightest pixel was mainly close to the direction of the impact in images made during the first 10-12 s, then quickly changed by about 50°, and then slowly became closer to the direction of the impact. The sharpest rays were caused by material ejected at $t_e \sim 20$ s. In particular, there were excessive ejections, especially in images at $t \sim 25$ -50 s after impact, in directions perpendicular to the direction of impact. Directions of excessive ejection could vary with time.

Acknowledgements

This work was supported by NASA DDAP grant NNX08AG25G to Catholic University of America and by NASA's Discovery Program Mission, Deep Impact, to the University of Maryland. The authors are extremely grateful to all the science team members, numerous engineers, scientists, and supporting people for making the mission possible and successful. We are thankful to reviewers for helpful discussion.

References

- A'Hearn, M.F., 2007. Deep Impact: excavating comet Tempel 1. *Highlights of Astronomy* 14, 325-326.
- A'Hearn, M.F., and 32 colleagues, 2005. Deep Impact: excavating comet Tempel 1. *Science* 310, 258-264.
- A'Hearn, M.F., Combi, M.R., 2007. Deep Impact at comet Tempel 1. *Icarus* 191, 1-3.
- A'Hearn, M.F., Belton, M.J.S., Collins, S.M., Farnham, T.L., Feaga, L.M., Groussin, O., Lisse, C.M., Meech, K.J., Schultz, P.H., Sunshine, J.M., 2008. Deep Impact and sample return. *Earth, Planets and Space* 60, 61-66.
- Barber, R.J., Miller, S., Stallard, T., Tennyson, J., Hirst, P., Carroll, T., Adamsov, A., 2007. The United Kingdom Infrared Telescope Deep Impact observations: Light curve, ejecta expansion rates and water spectral features. *Icarus* 187, 167-176.
- Bauer, J.M., Weissman, P.R., Choi, Y.-J., Troy, M., Young, J.W., Lisse, C.M., Dekany, R., Hanner, M.S., Buratti, B.J., 2007. Palomar and Table Mountain observations of 9P/Tempel 1 during the Deep Impact encounter: First results. *Icarus* 187, 296-305.
- Belton, M.J.S., and 14 colleagues, 2007. The internal structure of Jupiter family cometary nuclei from Deep Impact observations: The “talps” or “layered pile” model. *Icarus* 191, 571-585.
- Biver, N., and 16 colleagues, 2007. Radio observations of Comet 9P/Tempel 1 before and after Deep Impact. *Icarus* 187, 253-271.
- Busko, I., Lindler, D., A'Hearn, M.F., White, R.L., 2007. Searching for the Deep Impact crater on Comet 9P/Tempel 1 using image processing techniques. *Icarus* 187, 56-68.
- Cochran, A.L., Jackson, W.M., Meech, K., Glaz, M., 2007. Observations of Comet 9P/Tempel 1 with the Keck 1 HIRES instrument during Deep Impact, *Icarus* 187, 156-166.
- DiSanti, M.A., Villanueva, G.L., Bonev, B.P., Magee-Sauer, K., Lyke, J.E., Mumma, M.J., 2007. Temporal evolution of parent volatiles and dust in Comet 9P/Tempel 1 resulting from the Deep Impact experiment. *Icarus* 187, 240-252.
- Ernst, C.M., Schultz, P.H., A'Hearn, M. F., the Deep Impact Science Team, 2006. Photometric evolution of the Deep Impact flash. *Lunar Planet. Sci.* XXXVII, #2192 (abstract).

- Ernst, C.M., Schultz, P.H., 2007. Evolution of the Deep Impact flash: Implications for the nucleus surface based on laboratory experiments. *Icarus* 190, 334-344.
- Feldman, P.D., McCandliss, S.R., Route, M., Weaver, H.A., A'Hearn M.F., Belton, M.J.S., Meech, K.J., 2007. Hubble Space Telescope observations of Comet 9P/Tempel 1 during the Deep Impact encounter. *Icarus* 187, 113-122.
- Gault, D.E., Shoemaker, E.M., Moore, H.J., 1963. Spray ejected from the lunar surface by meteoroid impact. *NASA Tech. Note D-1767*.
- Harker, D.E., Woodward, C.E., Wooden, D.H., 2005. The dust grains from 9P/Tempel 1 before and after the encounter with Deep Impact. *Science* 310, 278-280.
- Harker, D.E., Woodward, C.E., Wooden, D.H., Fisher, R.S., Trujillo, C.A. 2007. Gemini-N mid-IR observations of the dust properties of the ejecta excavated from Comet 9P/Tempel 1 during Deep Impact. *Icarus* 190, 432-453.
- Hermalyn, B., Schultz, P.H., Anderson, J.L.B., Heineck, J.T., Time-resolved ejecta velocity distribution in oblique impacts. *10th conference "Asteroids, Comets, Meteors"* (Baltimore, USA, 14-18 July 2008), #8363 (abstract).
- Holsapple, K.A., 1993. The scaling of impact processes in planetary sciences. *Annu. Rev. Earth Planet. Sci.* 21, 333-373.
- Holsapple, K.A., Housen, K.R., 2007. A crater and its ejecta: An interpretation of Deep Impact. *Icarus* 187, 345-356.
- Housen, K.R., Schmidt, R.M., Holsapple, K.A., 1983. Crater ejecta scaling laws - Fundamental forms based on dimensional analysis. *J. Geophys. Res.* 88, 2485-2499.
- Ipatov, S.I., A'Hearn, M.F., 2006. Velocities of material ejected from Comet Tempel 1. *Lunar. Planet. Sci.* XXXVII, #1462 (abstract).
- Ipatov, S.I., A'Hearn, M.F., 2008a. Velocities of material ejected after the Deep Impact collision. *Lunar. Planet. Sci.* XXXIX, #1024 (abstract).
- Ipatov, S.I., A'Hearn, M.F., 2008b. Rate of ejection and velocities of material ejected from comet Tempel 1 after the Deep Impact collision. *DPS XL, BAAS 40*, 388-389.
- Ipatov, S.I., A'Hearn, M.F., 2009. Deep Impact ejection from Comet Tempel 1 as a triggered outburst. *Lunar. Planet. Sci.* XL, #1022 (abstract).
- Ipatov, S.I., Hahn, G.J., 1997. Evolution of the orbits of the objects P/1996 R2 (Lagerkvist) and P/1996 N2 (Elst-Pizarro). *Lunar. Planet. Sci.* XXVIII, #1590, pp. 619-620 (abstract).
- Ipatov, S.I., Hahn, G.J., 1999. Orbital evolution of the P/1996 R2 and P/1996 N2 objects, *Solar System Res.* 33, 487-500.
- Ipatov, S.I., Mather, J.C., 2003. Migration of trans-Neptunian objects to the terrestrial planets. *Earth, Moon, and Planets* 92, 89-98.
- Ipatov, S.I., Mather, J.C., 2004. Migration of Jupiter-family comets and resonant asteroids to near-Earth space. In: Belbruno, E., Folta, D., Gurfil, P. (Eds.), *Astrodynamics, Space Missions, and Chaos. Ann. N. Y. Acad. Sci.* 1017, 46-65, astro-ph/0308448.
- Ipatov, S.I., Mather, J.C., 2006. Migration of small bodies and dust to near-Earth space, *Adv. Space Res.* 37, 126-137.
- Ipatov, S.I., Mather, J.C., 2007. Migration of comets to the terrestrial planets. In: Milani, A., Valsecchi, G. B., Vokrouhlický, D. D. (Eds.), *Near-Earth Objects, Our Celestial Neighbors: Opportunity and Risk. IAU Symp.* No. 236, Prague, Czech Republic, 14-

- 18 Aug. 2006, pp. 55-64, astro-ph/0609721.
- Ipatov, S.I., A'Hearn, M.F., and Klaasen, K.P., 2007. Automatic removal of cosmic ray signatures on Deep Impact images, *Adv. Space Res.* 40, 160-172.
- Jehin, E., Manfroid, J., Hutsemekers, D., Cochran, A.L., Arpigny, C., Jackson, W.M., Rauer, H., Schulz, R., Zucconi, J.-M., 2006. Deep Impact: High-resolution optical spectroscopy with the ESO VLT and Keck I telescopes, *Astrophys. J.* 641, L145-L148.
- Jorda, L., Lamy, P., Faury, G., Keller, H.U., Hviid, S., Küppers, M., Koschny, D., Lecacheux, J., Gutierrez, P., Lara, L.M., 2007. Properties of the dust cloud caused by the Deep Impact experiment. *Icarus* 187, 208-219.
- Keller, H.U., and 11 colleagues, 2005. Deep Impact observations by OSIRIS onboard the Rosetta spacecraft. *Science* 310, 281-283.
- Keller, H.U., and 38 colleagues, 2007. Observations of Comet 9P/Tempel 1 around the Deep Impact event by the OSIRIS cameras onboard Rosetta. *Icarus* 187, 87-103.
- King, A., A'Hearn, M.F., Kolokolova, L., 2007. The properties of comet Tempel 1 as determined through the cometary ejecta. *Bull. AAS* 39, 449.
- Klaasen, K.P.; and 15 colleagues, 2007. Invited article: Deep Impact instrument calibration. *Review of Scientific Instruments* 79, 091301-091301-77.
- Knight, M.M., Walsh, K.J., A'Hearn, M.F., Swaters, R.A., Zauderer, B.A., Samarasinha, N.H., Valquez, R., Reitsema, H., 2007. Ground-based visible and near-IR observations of Comet 9P/Tempel 1 during the Deep Impact encounter. *Icarus* 187, 199-207.
- Koschny, D., Grün, E., 2001. Impacts into ice-silicate mixtures: ejecta mass and size distributions. *Icarus* 154, 402-411.
- Küppers, M., and 40 colleagues, 2005. A large dust/ice ratio in the nucleus of comet 9P/Tempel 1. *Nature* 437, 987-990.
- Lara, L.M., Boehnhardt, H., Gredel, R., Gutierrez, P.J., Rodrigo, R., Vindal-Nunez, M.J., 2007. Behavior of Comet 9P/Tempel 1 around the Deep Impact event, *Astron. Astrophys.* 465, 1061-1067.
- Li, J.-Y., and 10 colleagues, 2007. Deep Impact photometry of Comet 9P/Tempel 1. *Icarus* 187, 41-55.
- Lisse, C.M., and 16 colleagues, 2006. Spitzer spectral observations of the Deep Impact ejecta. *Science* 313, 635-640.
- Meech, K.J., and 208 colleagues, 2005. Deep Impact: Observations from a worldwide Earth-based campaign. *Science* 310, 265-269.
- Melosh, H.J., the Deep Impact Team, 2006. Deep Impact: The first second. *Lunar Planet. Sci.* XXXVII, #1165 (abstract).
- Meng, H., Zhang, L., Mei, L., Zhang, L., Zhai, M., Zhu, M., Shan, H., 2008. Optical observations of the outburst of Comet 17P/Holmes in its early phase. *10th conference "Asteroids, Comets, Meteors"* (Baltimore, USA, 14-18 July 2008), #8204 (abstract).
- Montalto, M., Riffeser, A., Hopp, U., Wilke, S., Carraro, G., 2008. The comet 17P/Holmes 2007 outburst: the early motion of the outburst material. *Astron. Astrophys.* 479, L45-L49.
- Petit, J.-M., Farinella, P., 1993. Modelling the outcomes of high-velocity impacts between small solar system bodies. *Celest. Mech. Dynam. Astron.* 57, 1-28.

- Richardson, J.E., Melosh, H.J., Artemeiva, N.A., Pierazzo, E., 2005. Impact cratering theory and modeling for the Deep Impact mission: From mission planning to data analysis. *Space Science Reviews* 117, 241-267.
- Richardson, J.E., Melosh, H.J., Lisse, C.M., Carcich, B., 2007. A ballistic analysis of the Deep Impact ejecta plume: determining comet Tempel 1's gravity, mass, and density. *Icarus* 190, 357-390.
- Schultz, P.H., Ernst, C.M., Anderson, J.L.B., 2005. Expectations for crater size and photometric evolution from the Deep Impact collision. *Space Science Reviews* 117, 207-239.
- Schultz, P.H., Eberhardy, C.A., Ernst, C.M., Sunshine, J.M., A'Hearn, M.F., Lisse, C.M., 2007. The Deep Impact oblique impact cratering experiment. *Icarus* 190, 295-333.
- Schleicher, D.G., Barnes, K.L., Baugh, N.F., 2007. Photometry and Imaging Results for Comet 9P/Tempel 1 and Deep Impact: Gas Production Rates, Postimpact Light Curves, and Ejecta Plume Morphology. *Astron. J.* 131, 1130-1137.
- Sugita, S., and 22 colleagues, 2005. Subaru telescope observations of Deep Impact. *Science* 310, 274-278.
- Sugita, S., and 12 colleagues, 2006. A high-resolution mid-IR observation of the collision between Deep Impact projectile and Comet Tempel 1. *Lunar Planet. Sci.* XXXVII, #2431 (abstract).
- Sunshine, J.M., Groussin, O., Schultz, P.H., A'Hearn, M.F., Feaga, L.M., Farnham, T.L., Klaasen, K.P., 2007. The distribution of water ice in the interior of Comet Tempel 1. *Icarus* 190, 284-294.
- Tozzi, G.P., and 16 colleagues, 2007. Dust observations of Comet 9P/Tempel 1 at the time of the Deep Impact. *Astron. & Astrophys.* 476, 979-988.
- Walker, R.G., Weaver, W.B., Shane, W.W., Babcock, A., 2007. Deep Impact: Optical spectroscopy and photometry obtained at MIRA. *Icarus* 187, 285-295.
- Yamamoto, S., Nakamura, A.M., 1997. Velocity measurements of impact ejecta from regolith targets. *Icarus* 128, 160-170.
- Yamamoto, S., Kadono, T., Sugita, S., Matsui, T., 2005. Velocity distributions of high-velocity ejecta from regolith targets. *Icarus* 178, 264-273.

Figure captions

Fig. 1. Variation of pixel scale (in meters) with time (in seconds) for HRI images.

Fig. 2. Variation of the relative brightness Br of the brightest pixel with time t (in seconds). It is considered that $Br=1$ at $t=4$ s. Series of images Ma , Mb , Ha , Hb , Hc , Hd , and He are described in Table 2. Plot (b) is a part of plot (a) and allows one to see variations at $t>10$ s in more detail.

Fig. 3. (a) Coordinates x and y of the brightest pixel in MRI (series Ma) and HRI (series Ha) images relative to the position of the brightest pixel in the MRI image at $t=0.001$ s (the place of impact) at different times after the impact. The difference in brightness between a current image and an image before the impact was considered. Coordinates are given in HRI pixels (i.e., the number of MRI pixels was multiplied by a factor of 5). HRI y -plot relative to the position of the brightest pixel in the HRI image at $t=0.215$ s (the place of ejection of material at $t\geq 0.2$ s) was shifted down by 5 pixels to

consider the position of the brightest pixel relative to the place of impact. (b) The angle (in degrees) of the direction from the brightest pixel at $t=0.215$ s (close to the place of ejection) to the brightest pixel at a current time for HRI images from series *Ha* and *Hc*. The angle corresponding to the direction of the impact was about -60° .

Fig. 4. Contours for the difference in brightness between MRI images (series *Ma*) made 0.993, 1.986, 2.978 (upper row), 3.970, 4.962, and 5.720 s (lower row) after the impact and the image at $t=-0.057$ s. The contours correspond to constant calibrated physical surface brightness (CPSB, in $\text{W m}^{-2} \text{sterad}^{-1} \text{micron}^{-1}$) equal to 3, 1, 0.3, and 0.1, respectively. A large cross shows the position of the brightest pixel at $t=0.06$ s, and a smaller cross, at current time.

Fig. 5. Contours corresponding to CPSB equal to 3, 1, 0.3, and 0.1 for the difference in brightness between HRI (High Resolution Instrument) images from series *Ha* made 1.852 (a), 4.379 (b), 8.00 s (c), 12.254 s (d), 16.524 s (e), and 20.906 s (f) after the impact and the image at $t=-0.629$ s. The largest cross shows the position of the brightest pixel at $t=0.215$ s, and a smaller cross, at current time. The size of a cross indicating the position of the brightest pixel at current time is smaller for a greater value of time.

Fig. 6. Contours corresponding to CPSB equal to 3 (a) and 1 (b), for the difference in brightness between HRI images from series *Ha* made 1.852, 4.379, 8.00, 12.254, 16.524, and 20.906 s after the impact and the image at $t=-0.629$ s. Contours corresponding to CPSB equal to 3 (c) and 1 (d), for the difference in brightness between *Ha* images made 1.008, 1.852, 25.332, 30.00, 35.715, 42.618, and 109.141 s after the impact and the image at $t=-0.629$ s. The contour at $t=109$ s is the third from the place of impact, and other contours are larger for larger times. The largest cross shows the position of the brightest pixel at $t=0.215$ s. The size of a cross indicating the position of the brightest pixel at current time is smaller for a greater value of time.

Fig. 7. Contours corresponding to CPSB equal to 3, 1.5, 1, and 0.5, for HRI images from series *Hb* made 39.274 (a), 66.176 (b), 142.118 (c), 384.561 (d), 529.37 (e), and 665 s (f) after the impact. The position of the brightest pixel in an image is marked by a cross.

Fig. 8. Contours corresponding to CPSB equal to 1, 0.3, 0.1, and 0.03, for MRI images from series *Mb* made 77.651 (a), 138.901 (b), 191.53 (c), 311.055 (d), 351.043 (e), and 410.618 s (f) after the impact. The position of the brightest pixel in an image is marked by a cross.

Fig. 9. Difference in brightness between MRI (Medium Resolution Instrument) images (series *Ma*) made 0.060, 0.165, 0.224, 0.282, 0.341 (upper row), 0.400, 0.462, 0.579, 0.697, and 0.814 s (lower row) after the impact and the image at $t=-0.057$ s. In figure (a) a white region corresponds approximately to constant calibrated physical surface brightness $\text{CPSB} \geq 3$ (in $\text{W m}^{-2} \text{sterad}^{-1} \text{micron}^{-1}$), and in figure (b) it corresponds to $\text{CPSB} \geq 0.5$, but both figures present the same images.

Fig. 10. Variations of sizes L (in km) of regions inside contours of $\text{CPSB}=\text{const}$ with time t (in seconds). Series of images *Ma*, *Mb*, *Ha*, *Hb*, *Hc*, *Hd*, and *He* are described in Table 2. The number after a designation of the series in the figure legend shows the value of CPSB for the considered contour. For series *Ma*, we considered L as the distance from the place of impact to the contour down in y -direction. For other series, we considered the difference between maximum and minimum values of x for the contour.

Fig. 11. Typical projections v_{model} of velocities (in km s^{-1}) onto the plane perpendicular to a line of sight at time t_e of ejection for the model when velocities v_{model} at t_e are the same as velocities $v_{\text{expt}}=c \times (t/0.26)^{-\alpha}$ of the edge of the bright region observed at time t , for four pairs of α and c . The distance from the place of ejection to the edge was used to find the dependence of t on t_e . The size of the bright region was analyzed (see Section 5) based on the contours CPSB=3 at time t for series *Ma*, *Ha*, *Hb*, *Hd*, and *He*, and CPSB=1.75 for series *Mb*. $v_{y\text{obs}}$ and $v_{x\text{obs}}$ are our estimates of the projection $v_p(t_e)$ of velocity that were based mainly on analysis of minima and maxima of the plots presented in Fig. 10 for y -direction and x -direction, respectively. v_{ray} shows two estimates of $v_p(t_e)$ obtained at analysis of rays of ejected material in Section 7. The values of $v_{y\text{min}}$ and $v_{x\text{min}}$ show the minimum velocities needed to reach the edge of the bright region (considered at time t) from the place of ejection moving in y or x -direction, respectively. Four curves $v_{\text{expt}}=c \times (t/0.26)^{-\alpha}$ with different values of α and c are also presented. Note that v_{expt} and v_{model} depend on t and t_e , respectively.

Fig. 12. Ratio of time t_e of ejection to time t for the model for which velocities v_{model} at t_e are the same as velocities $v_{\text{expt}}=c \times (t/0.26)^{-\alpha}$ of the edge of the observed bright region at time t , for four pairs of α and c . Plusses “+” show the values of the ratio based on analysis of minima and maxima of the plots presented in Fig. 10.

Fig. 13. Time variations of the relative values V_r of the volume of the bright region close to the place of ejection and of the relative rate of ejection $V_r \times t^{-\alpha}$ (which is proportional to $V_r \times v_t$) for the model in which velocities v_t of ejected material are proportional to $t^{-\alpha}$, at four values of α . It is considered that $V_r=1$ at $t=1$ s.

Fig. 14. Relative rate r_{te} of ejection at different times t_e of ejection for the model in which characteristic velocities of the edge of the observed bright region at time t are equal to $v_{\text{expt}}=c \times (t/0.26)^{-\alpha}$, for four pairs of α and c . Maximum values of the rates are considered to be equal to 1. Five curves of the type $y=c_r \times (x-c_t)^\beta$ are also presented for comparison. In figure (b) we present a part of figure (a).

Fig. 15. Relative volume f_{et} of observed material ejected before time t_e vs. t_e for the model in which characteristic velocities of the edge of the observed bright region at time t are equal to $v_{\text{expt}}=c \times (t/0.26)^{-\alpha}$, for four pairs of α and c . $f_{et}=1$ for material ejected before t_e corresponding to the edge of the bright region at $t=803$ s. Three curves of the type $f_{et}=c_r \times (x-c_t)^\beta$ are also presented for comparison.

Fig. 16. Relative volume f_{ev} of material ejected with velocities greater than v vs. v for the model in which characteristic velocities of the edge of the observed bright region at time t are equal to $v=v_{\text{expt}}=c \times (t/0.26)^{-\alpha}$, for five pairs of α and c . $f_{ev}=1$ for material ejected before t_e corresponding to the edge of the bright region at $t=803$ s. Five curves of the type $f_{ev}=c_r \times x^\beta$ are also presented for comparison.

Table 1

Projection of velocity (in m s^{-1}) of the leading edge of the DI dust cloud of ejected material onto the plane perpendicular to the line of sight at several moments of time and the mass of ejected material (in kg) obtained at different observations

Source	Telescope	Resolution, km pixel ⁻¹	Considered time t after the impact	Projected velocity at t , m s^{-1}	Total mass of ejected material with diameter d , kg
Harker et al. (2005, 2007)	8.1-m Frederick C. Gillette (Gemini-N) telescope on Mauna Kea, Hawaii; MICHELLE imaging spectrograph, 7.8-13 μm	388	1 h	220 – grains with $d \sim 0.4 \mu\text{m}$	$(7.3-8.4) \times 10^4$ – dust with $d < 2 \mu\text{m}$; 1.5×10^6 – dust with $d < 200 \mu\text{m}$;
Küppers et al. (2005)	Rosetta, OSIRIS camera	1500	40 min	> 110 ; 300 - fine dust	4.4×10^5 – dust with $d < 2 \mu\text{m}$; 10^7 – water and dust; 4.5×10^6 – water
Meech et al. (2005)	Many ground-based telescopes		20 h	200	10^6 - dust with typical $d \sim 1 \mu\text{m}$
Ipatov and A'Hearn (2006)	Deep Impact, MRI	0.087	8-15 s	200; 100 – the brightest material	
Jehin et al. (2006)	Keck I telescope (10 m) on Mauna Kea (Hawaii), High Resolution Echelle Spectrometer (HIRES)		4 h	150 – dust; 400 - gas CN	
Lisse et al. (2006), supplemental on-line material	Spitzer Space Telescope, Infrared Spectrograph, 5-35 μm	550	45 min	200-300	2.2×10^5 – dust at $d < 2 \mu\text{m}$ 7.8×10^5 – dust at $d < 20 \mu\text{m}$ 9.9×10^5 – dust at $d < 2 \text{ mm}$; 5.8×10^5 – water
Sugita et al. (2005, 2006)	8.2 m Subaru telescope and its mid-infrared detector, COMICS, 8.8-24.5 μm		1 h	125	$(5.6-8.5) \times 10^5$ - dust with $d < 20 \mu\text{m}$ $(2.8-7.0) \times 10^7$ - dust and bodies with $d < 2 \text{ m}$
Schleicher et al.	Hall telescope (1.1 m) and Lowell's	765	23 h	220	$\leq 1.3 \times 10^7$ - water

(2006)	telescope (0.8 m)				
Barber et al. (2007)	United Kingdom Infrared Telescope (3.8 m) on Mauna Kea, Hawaii; spectrometer CGS4		110 min 20 h	125 260	
Bauer et al. (2007)	Palomar 200-inch telescope, near-IR PHARO camera		75 min	200	2×10^5 – dust at $d \sim 1.4 \mu\text{m}$
Biver et al. (2007)	Nançay, IRAM and CSO radio telescopes, Odin satellite			350 - water	5×10^6 – water
Cochran et al. (2007)	Keck I telescope (10 m) on Mauna Kea (Hawaii), HIRES spectrograph		75 min	510 - gas CN	
Feldman et al. (2007)	Hubble Space Telescope, Advanced Camera for Surveys, V filter, $0.6 \mu\text{m}$	16	75-100 min	70-80 – the most probable; 115 – mean expansion speed; 145 – rms velocity	
Jorda et al. (2007)	Rosetta, OSIRIS camera, Orange filter ($0.645 \mu\text{m}$)	1500	10 d	Peak at 190 with FWHM=150	1.5×10^5 – dust with $d < 2.8 \mu\text{m}$; $(1-14) \times 10^6$ – dust with $d < 200 \mu\text{m}$
Keller et al (2005, 2007)	Rosetta, OSIRIS camera ($0.245-1 \mu\text{m}$)	1500	4 h (1.42 – 3.73 days to estimate the mass)	200	1.6×10^5 – dust with $d < 2.8 \mu\text{m}$; $(1-14) \times 10^6$ – dust with $d < 200 \mu\text{m}$; $(4.5-9) \times 10^6$ – water
Knight et al. (2007)	Kitt Peak Nat. Observatory (2.1 m telescope, SQUID IR camera, $1.1-3.3 \mu\text{m}$) and Observ. Astron. Nac.-San Pedro Martir (1.5 m telescope)	447	24 h	200-230	

Lara et al. (2007)	2 m telescope at Calar Alto Observatory, instrument CAFOS, 2.8-10 μm		15 h 40 h	230 150	$\geq 1.2 \times 10^6$ – dust
Tozzi et al. (2007)	European Southern Observatory, La Silla and Paranal sites, near-IR		20 h	115 – average with a FWHM=75	
Walker et al. (2007)	36-inch telescope at MIRA's Bernard Oliver Observing Station		50 min 25 h	230 185	
Ipatov and A'Hearn, the present paper	Deep Impact, MRI; Deep Impact, HRI	0.087; 0.017	13 min	100-200	

Table 2

Series of images considered. Instrument (telescope) used, total integration time (INTTIME, in seconds), size of considered images (in pixels), exposure ID (EXPID), and time after impact (IMPACTM, in seconds). For all images CLEAR filter was used. For series *Ma*, the image number within commanded exposure (IMGNUM) varied from 64 to 156. For series *Ma*, *Ha*, and *Hc*, we analyzed the differences in brightness between a current image and that before the impact (the MRI image with EXPID=910 and IMGNUM=63 made at $t=-0.057$ s, or the HRI image with EXPID=9000910 and IMGNUM=5 made at $t=-0.629$). These series are marked by “(dif)”. For other series, the brightness in current images was analyzed.

Series	Instru- ment	INTTIME, seconds	Size, pixels	EXPID	IMPACTM, seconds
				min, max	min, max
<i>Ma</i> (dif)	MRI	0.0514	64×64	9000910, 9000910	0.001, 5.720
<i>Mb</i>	MRI	0.3	1024×1024	9000942, 9001067	77.651, 802.871
<i>Ha</i> (dif)	HRI	0.1	512×512	9000910, 9000945	0.215, 109.141
<i>Hb</i>	HRI	0.6	1024×1024	9000931, 9001002	39.274, 664.993
<i>Hc</i> (dif)	HRI	0.6	512×512	9000927, 9000942	27.664, 86.368
<i>Hd</i>	HRI	0.1	1024×1024	9000934, 9000961	50.715, 251.525
<i>He</i>	HRI	0.5	1024×1024	9001017, 9001036	719.805, 771.95

Table 3

Estimated time of ejection t_e and x and y projections (v_{px} and v_{py}) of velocity v_p of ejection obtained based on analysis of sizes of contours CPSB=const for times t_1 and t_2 . The ratio t_e/t_1 is presented if at t_1 the closest contour (usually CPSB=3) was considered.

t_e	0.2	0.26	1.44	4.4	10	15	17	21	73	90	100	115
t_1	0.224	0.34	2.74	8	55.6	30	55.6	31	120	120	140	140
t_2	0.282	0.46	4.96	12.2	100.4	56	100.4	56	170	170	410	410
t_e/t_1	0.89	0.76	0.53	0.55		0.5		0.68	0.61	0.75	0.71	0.82
v_{px}					95			105		25	20	
v_{py}	7500	1500	930	240		105	105		16			26

Table 4

Exponents of the time dependences of the ejection velocity v , the relative rate r_{te} of ejection, and the relative volume f_{et} of observed material ejected before time t_e , and exponents of the velocity dependence of the relative volume f_{ev} of material ejected with velocities greater than v .

v	r_{te}	f_{et}	f_{ev}	the cratering event is primarily governed by	material
$t_e^{-0.75}$	$t_e^{-0.25}$	$t_e^{0.75}$	v^{-1}	the impactor's momentum	
$t_e^{-0.71}$	$t_e^{-0.13}$	$t_e^{0.87}$	$v^{-1.23}$		sand
$t_e^{-0.644}$	$t_e^{0.07}$	$t_e^{1.07}$	$v^{-1.66}$		Soft rock
$t_e^{-0.6}$	$t_e^{0.2}$	$t_e^{1.2}$	v^{-2}	the impactor's kinetic energy	basalt

Table 5

Characteristics of our model of ejection for several pairs of α and c (see Sections 5-6). Designations: t_{e803} is the value of time t_e of ejection corresponded to the bright region at $t=803$ s, v_{e803} is the ejection velocity at t_{e803} , t_{elm} is the ejection time corresponded to the local peak of ejection rate, f_1 is the fraction of material ejected during the first second, f_{ev200} is the fraction of material ejected with velocity $v_p \geq 200$ m s⁻¹, f_{ev100} is the fraction of material ejected with velocity $v_p \geq 100$ m s⁻¹; t_{ev200} and t_{ev100} are the values of the time of ejection corresponded to f_{ev200} and f_{ev100} , respectively; t_{et05} is the time during which a half of material observed during 800 s was ejected, v_{et05} is the limit of velocity corresponded to t_{et05} .

α	0.6	0.644	0.71	0.75	0.75	0.75
c	2	2	2.5	3	2.5	2
t_{e803} , s	728	696	658	636	603	553
v_{e803} , m s ⁻¹	16	11	8	7	6	5
t_{elm} , s	13	11	11	11	9	6
f_1	0.01	0.014	0.017	0.018	0.022	0.037
f_{ev200}	0.05	0.05	0.07	0.08	0.07	0.065
f_{ev100}	0.22	0.18	0.17	0.19	0.12	0.09
t_{ev200} , s	8.4	6	6	6	4.2	3
t_{ev100} , s	29.5	18	14.5	14.6	9	5.5
t_{et05} , s	226	199	140	111	105	68
v_{et05} , m s ⁻¹	32	25	25	25	23	23

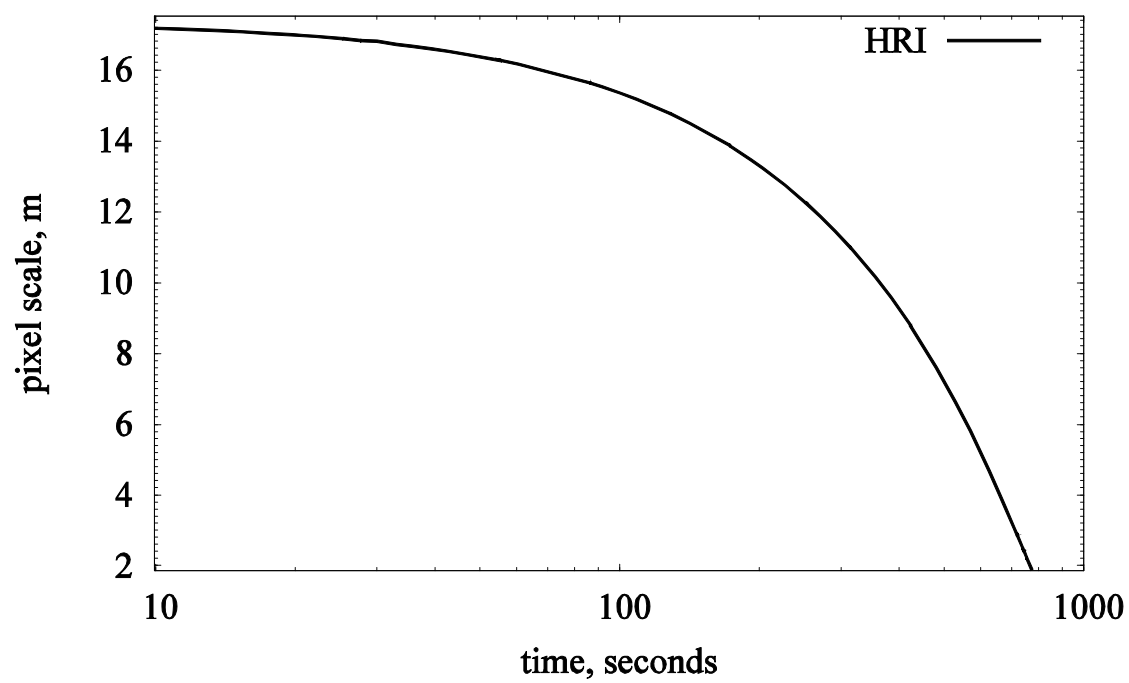
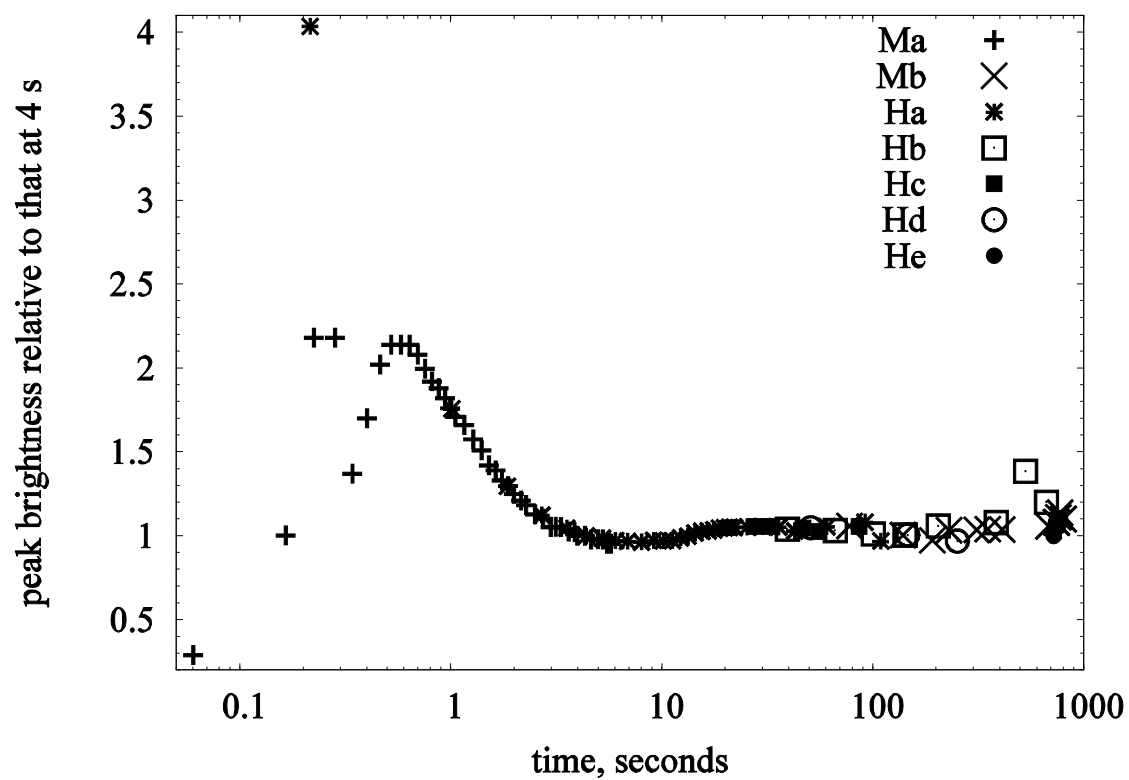
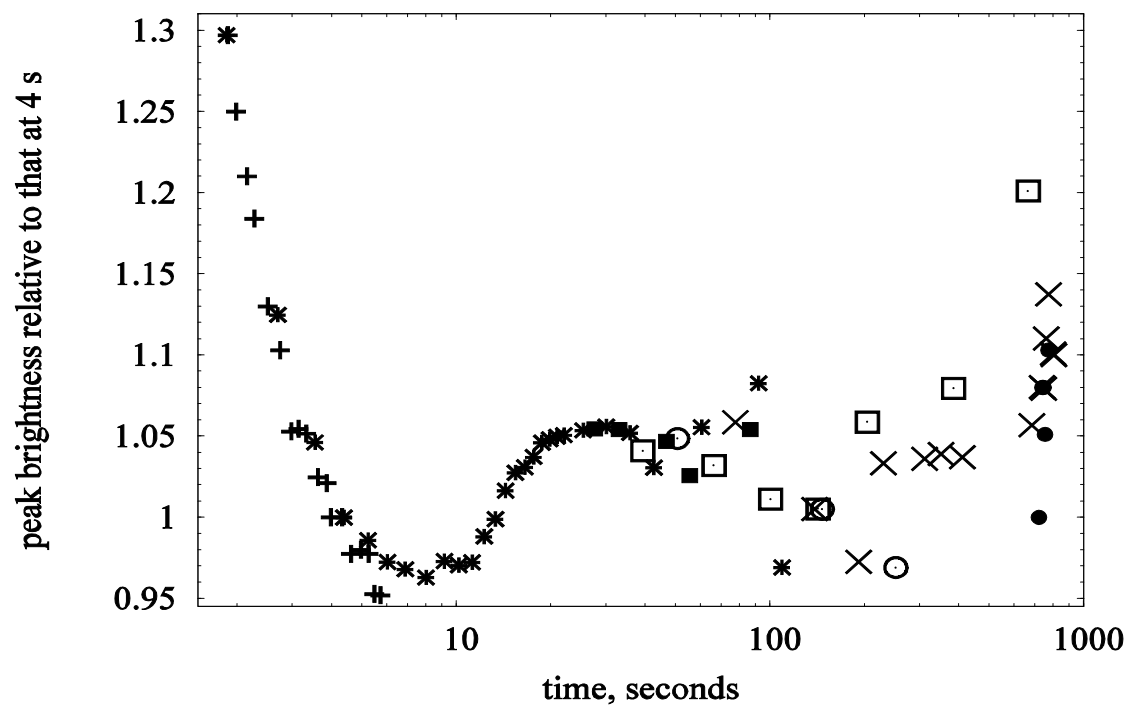


Fig. 1

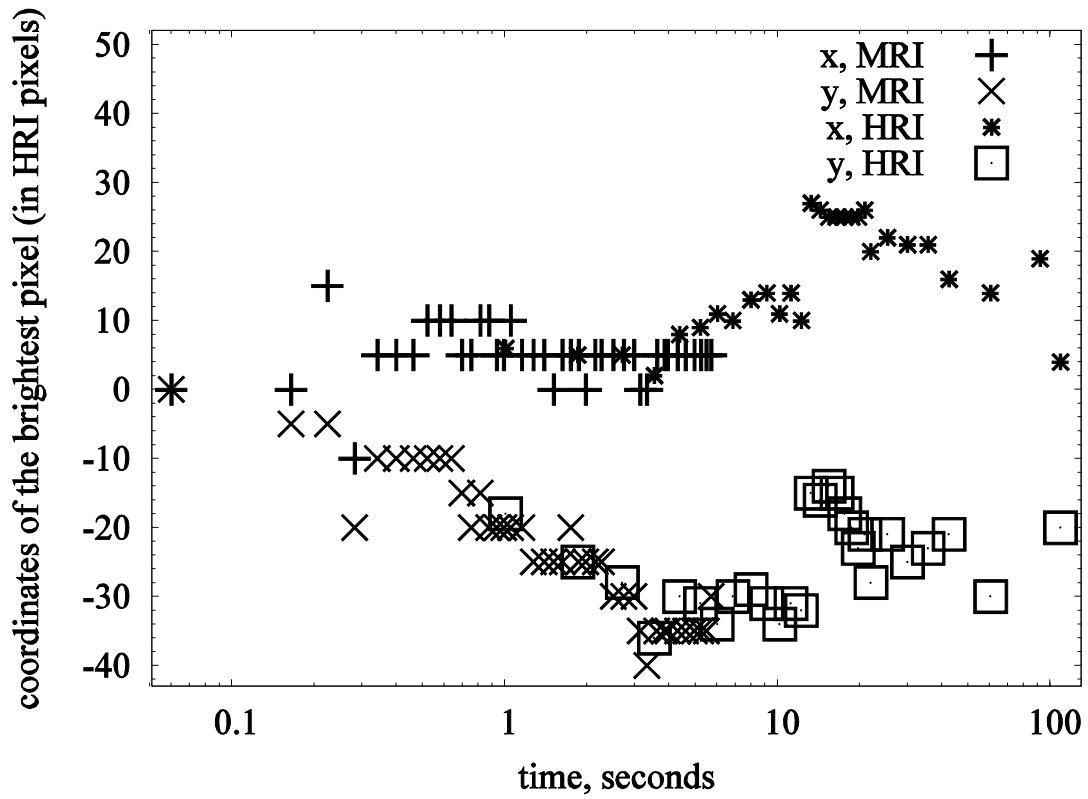


(a)

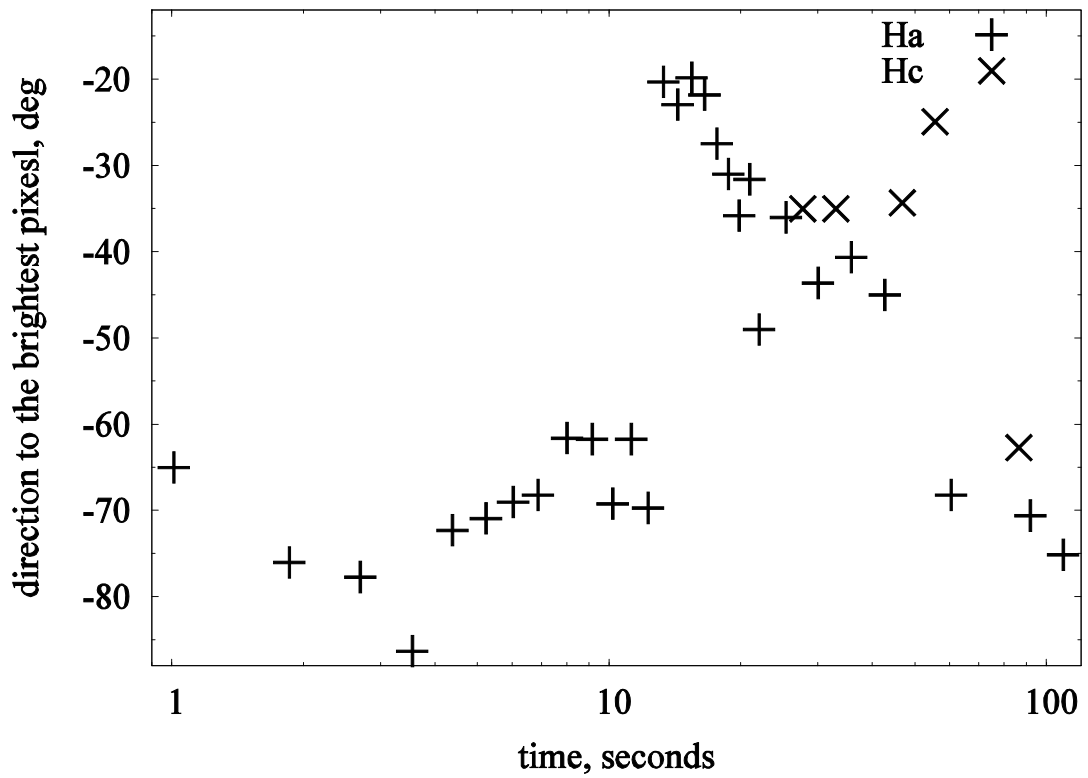


(b)

Figure 2



(a)



(b)

Figure 3

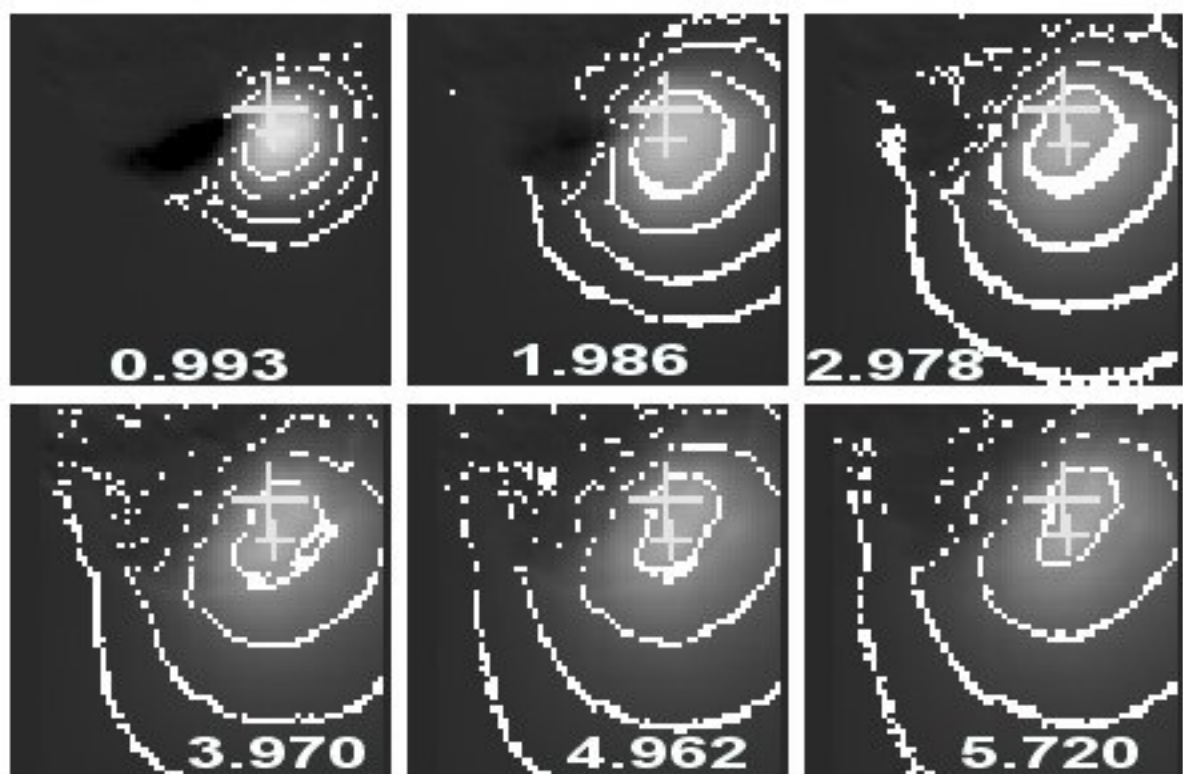


Figure 4

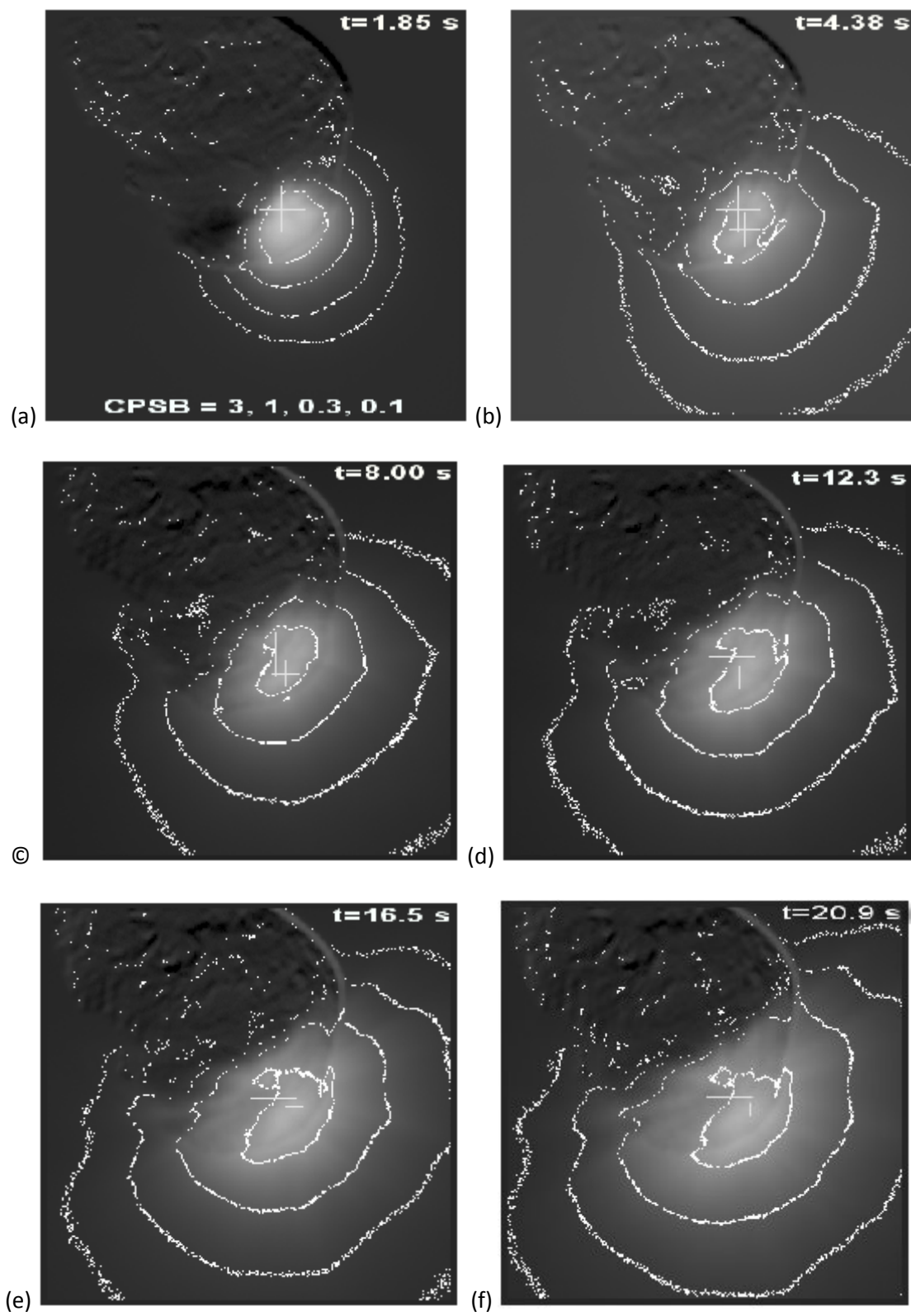


Figure 5

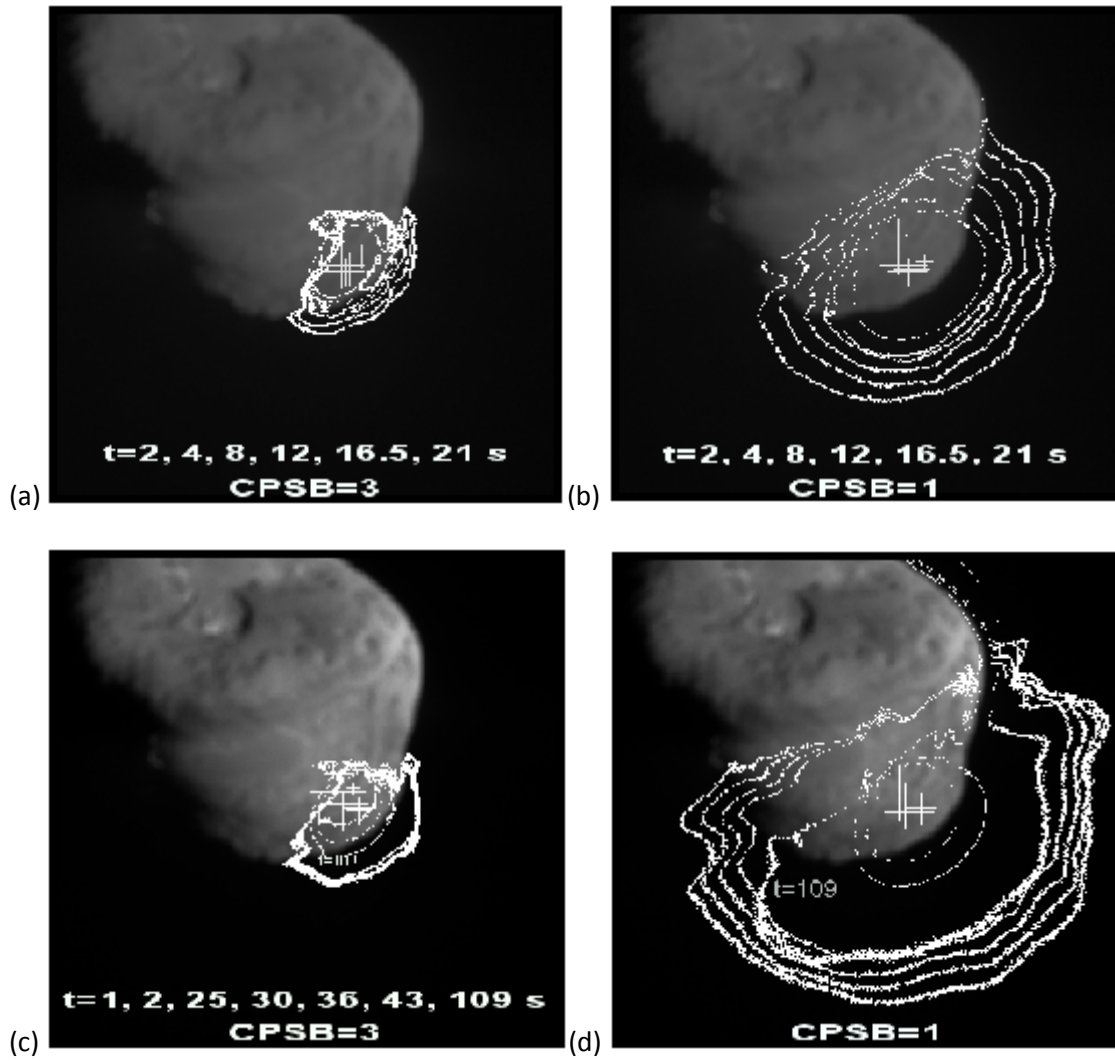


Figure 6

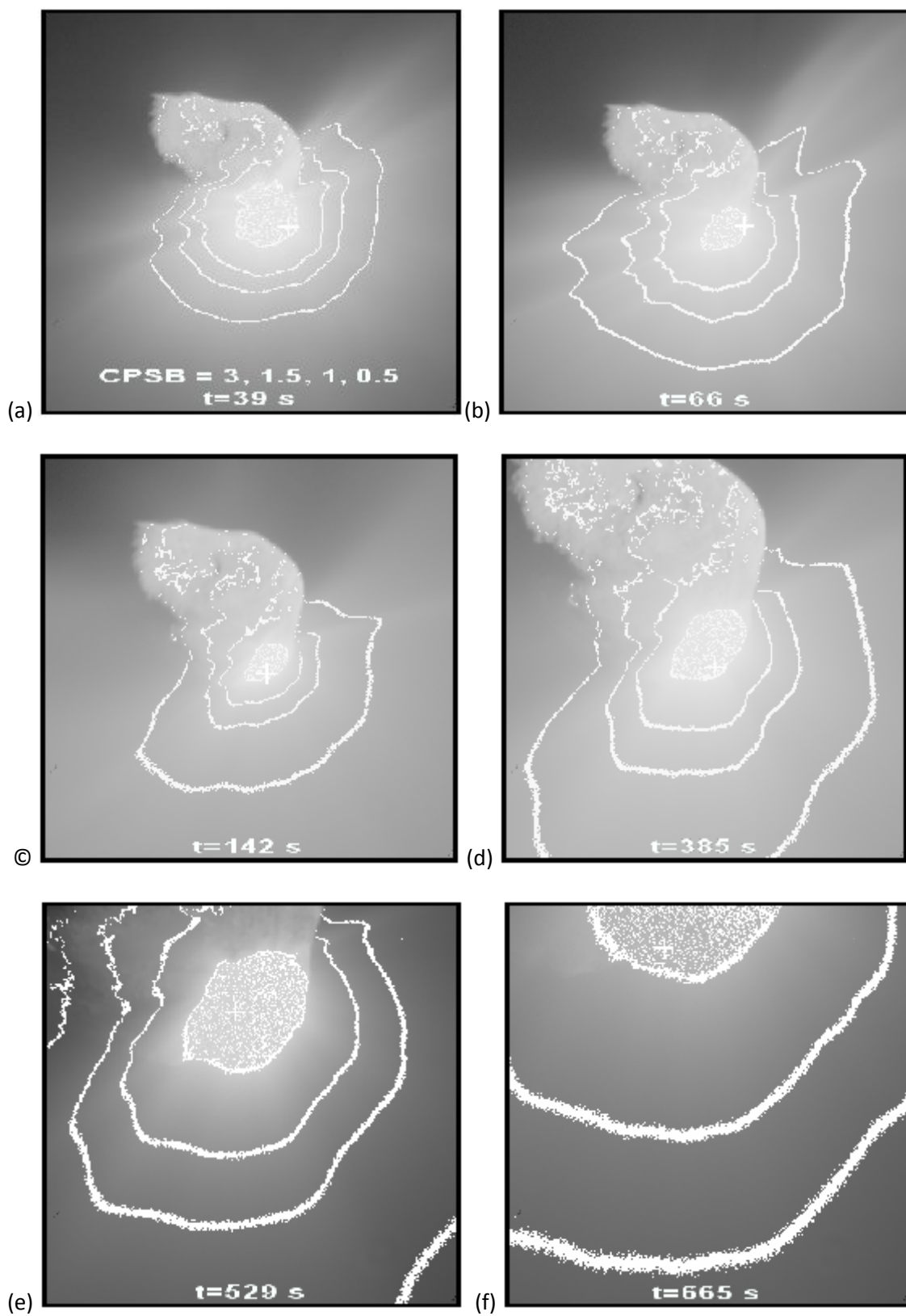


Figure 7

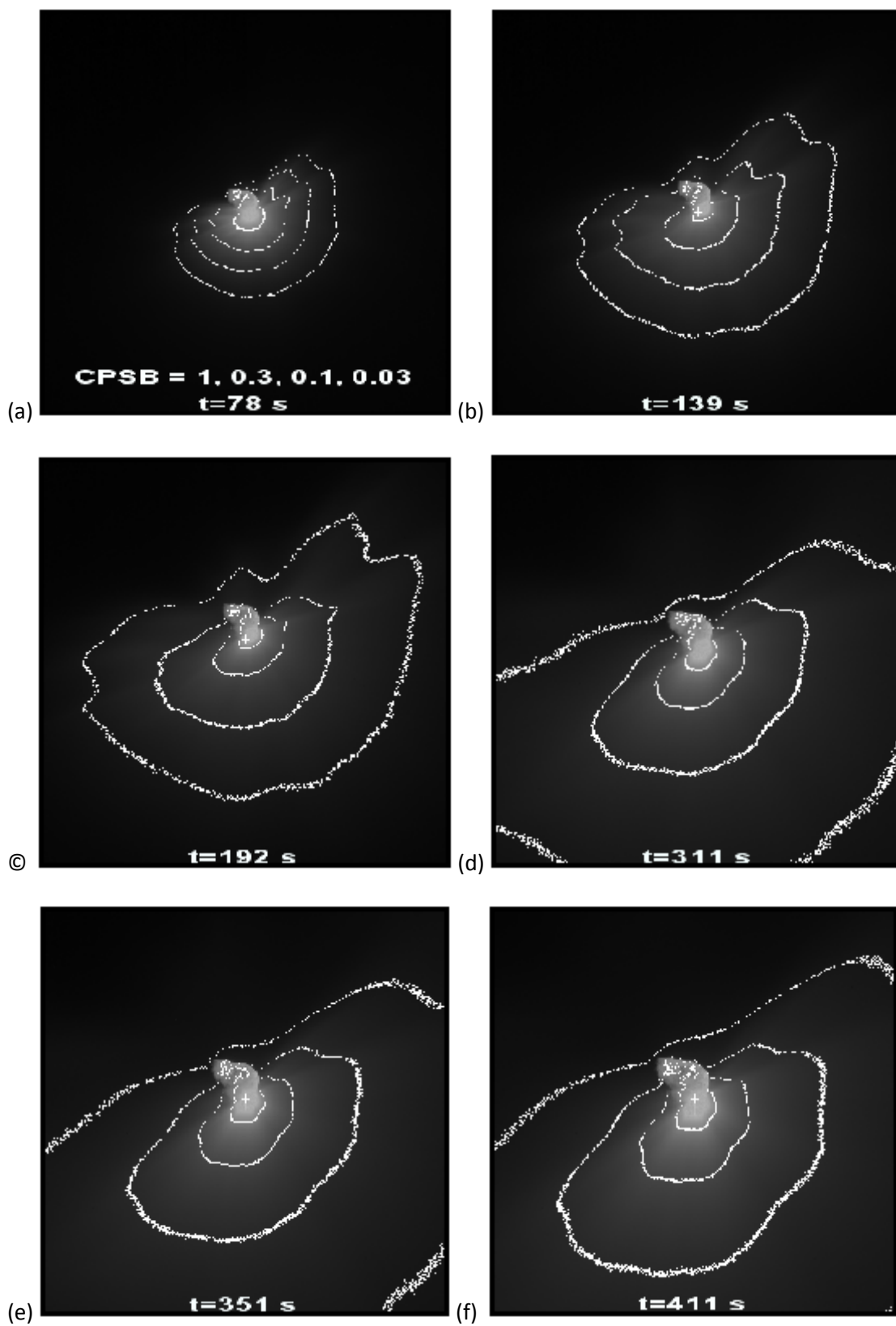
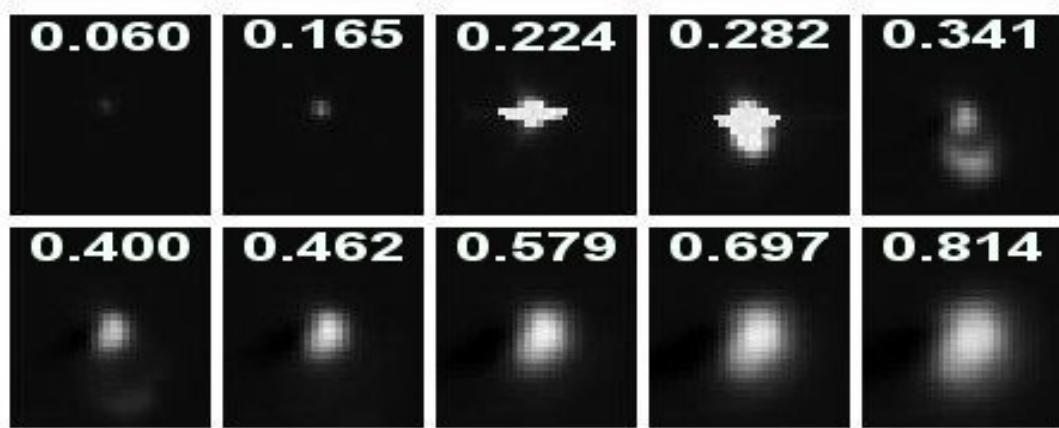
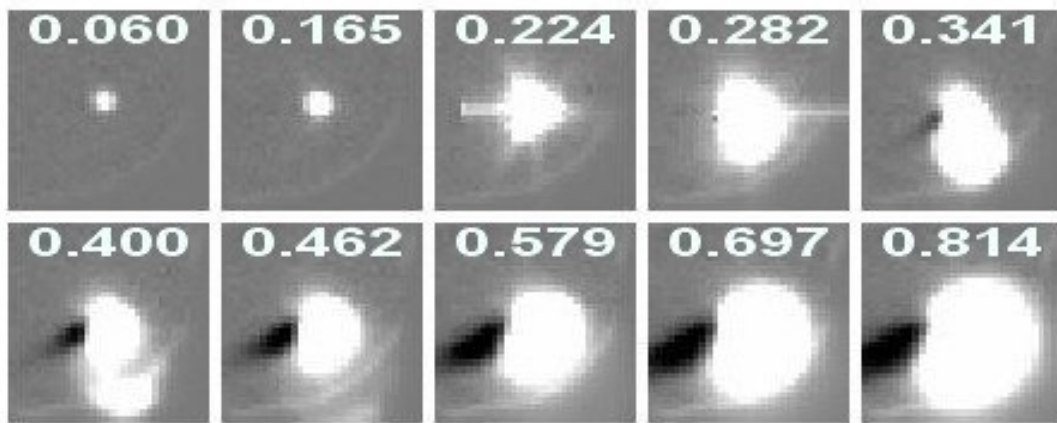


Figure 8



(a)



(b)

Figure 9

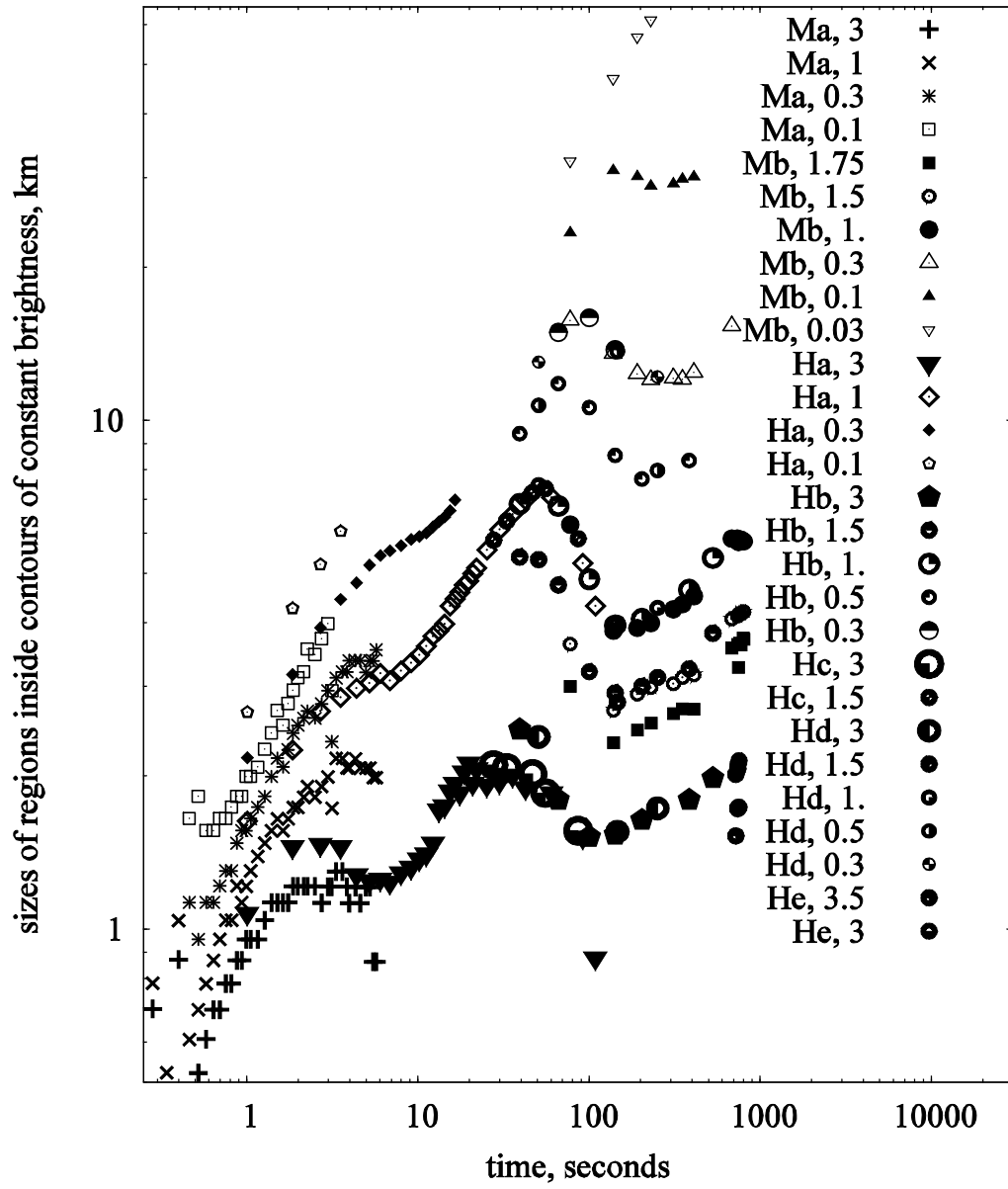


Figure 10

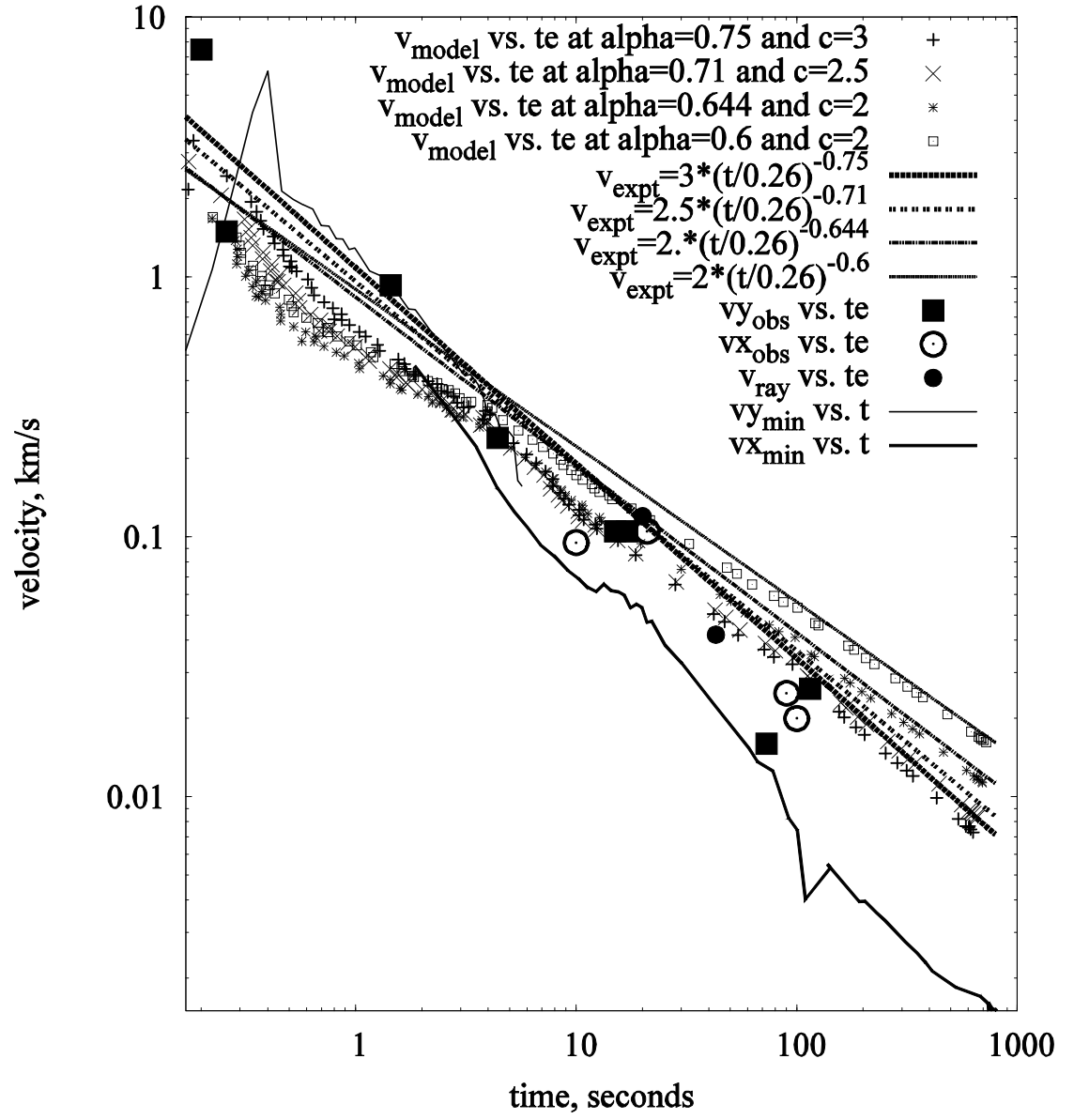


Fig. 11

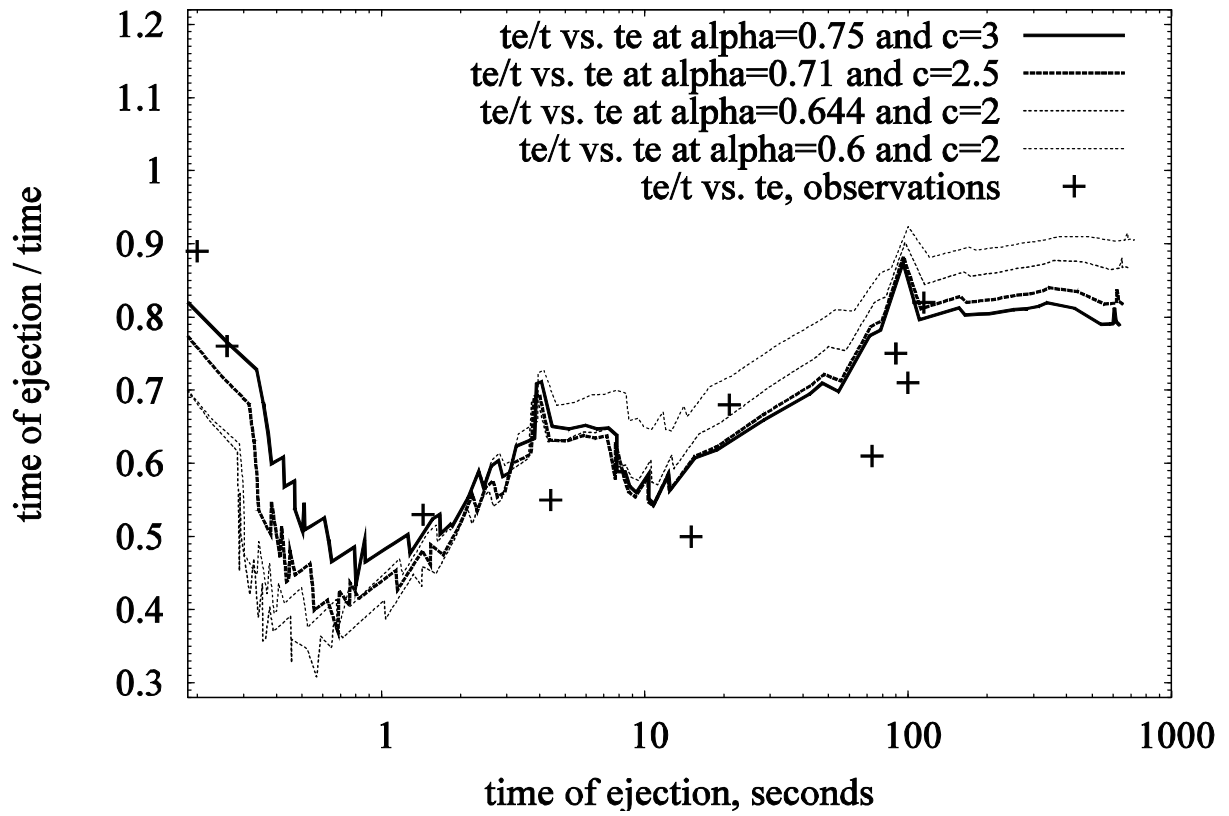


Figure 12

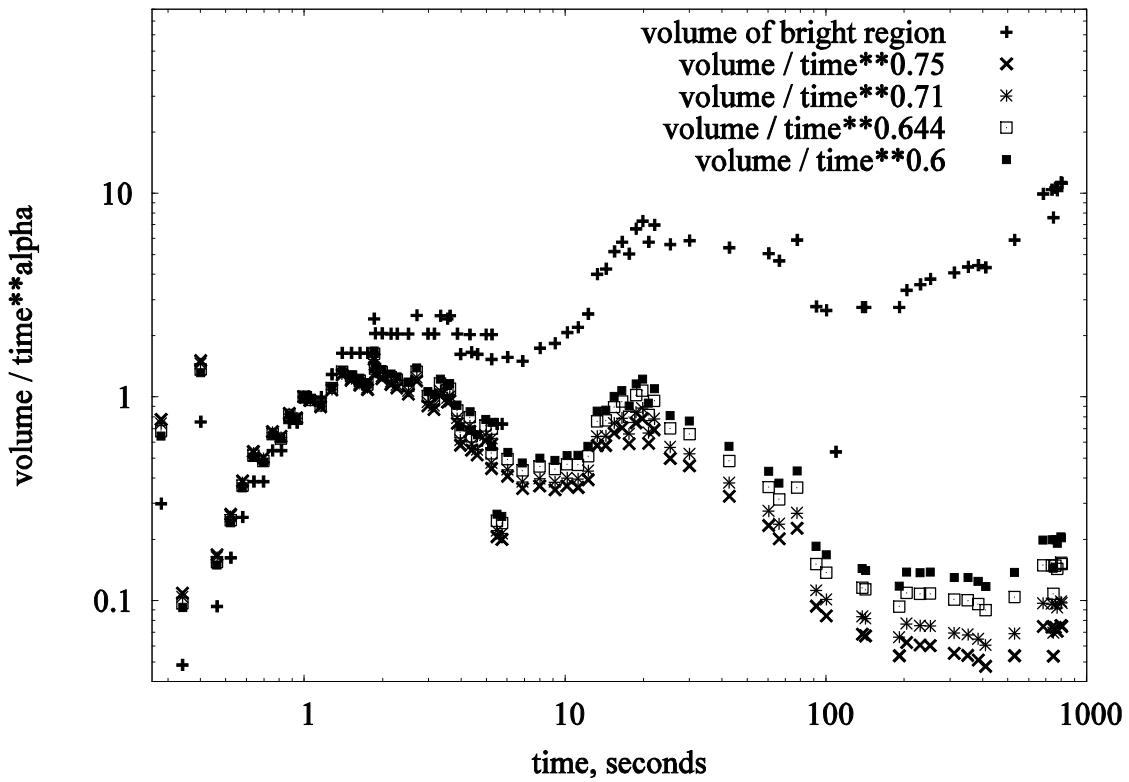
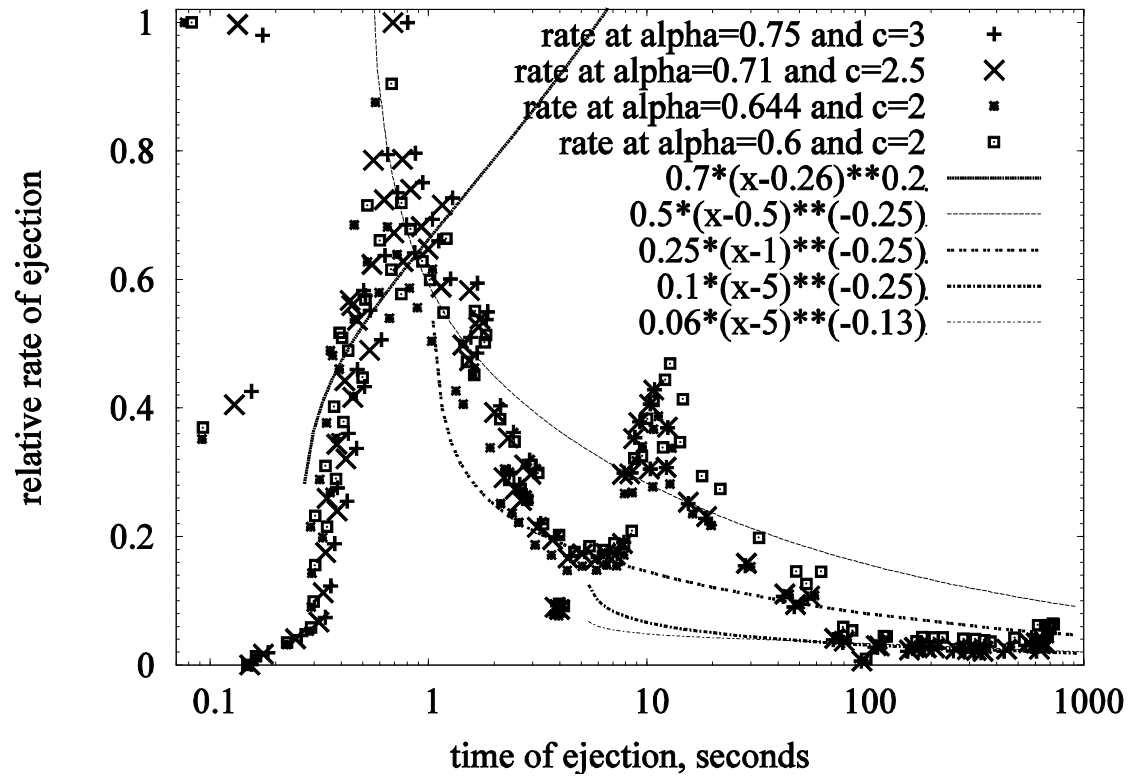
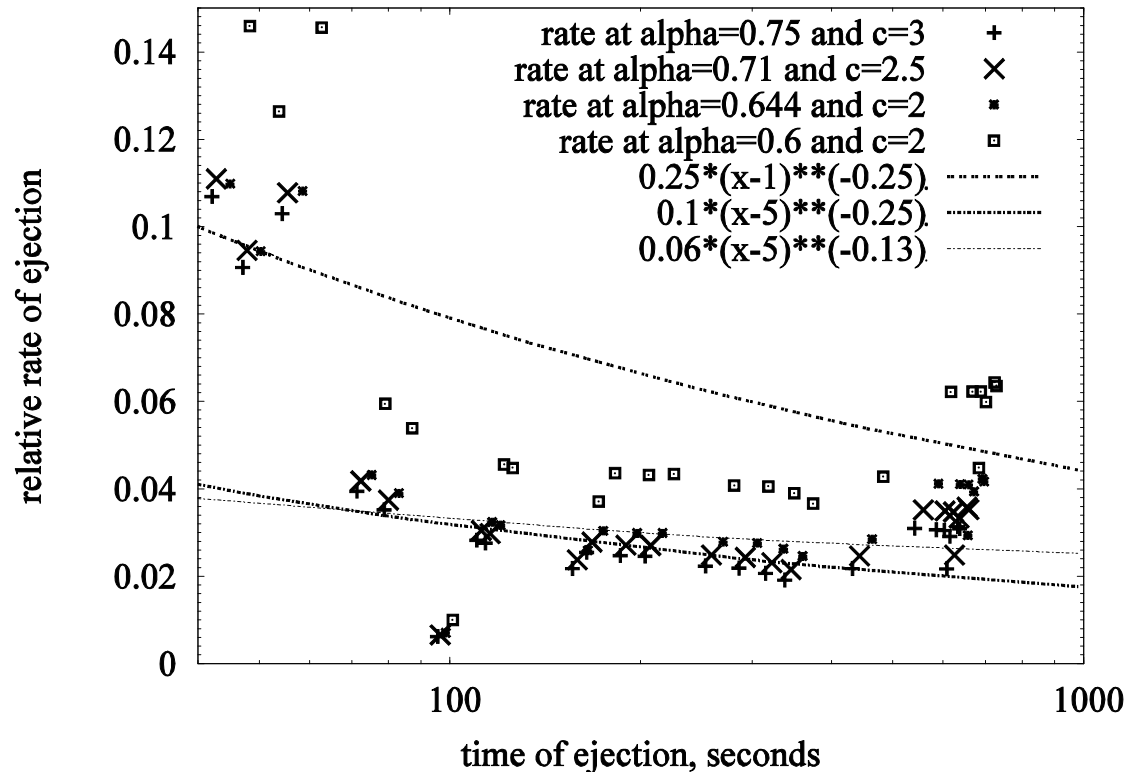


Figure 13



(a)



(b)

Fig. 14

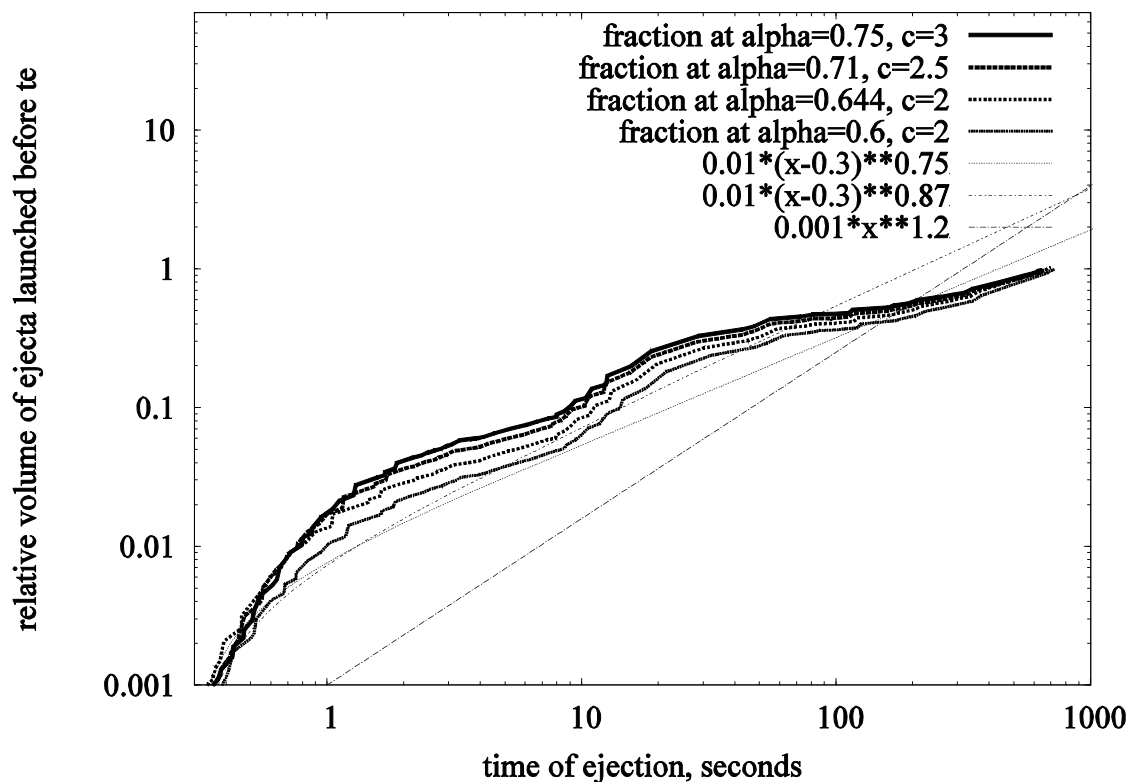


Figure 15

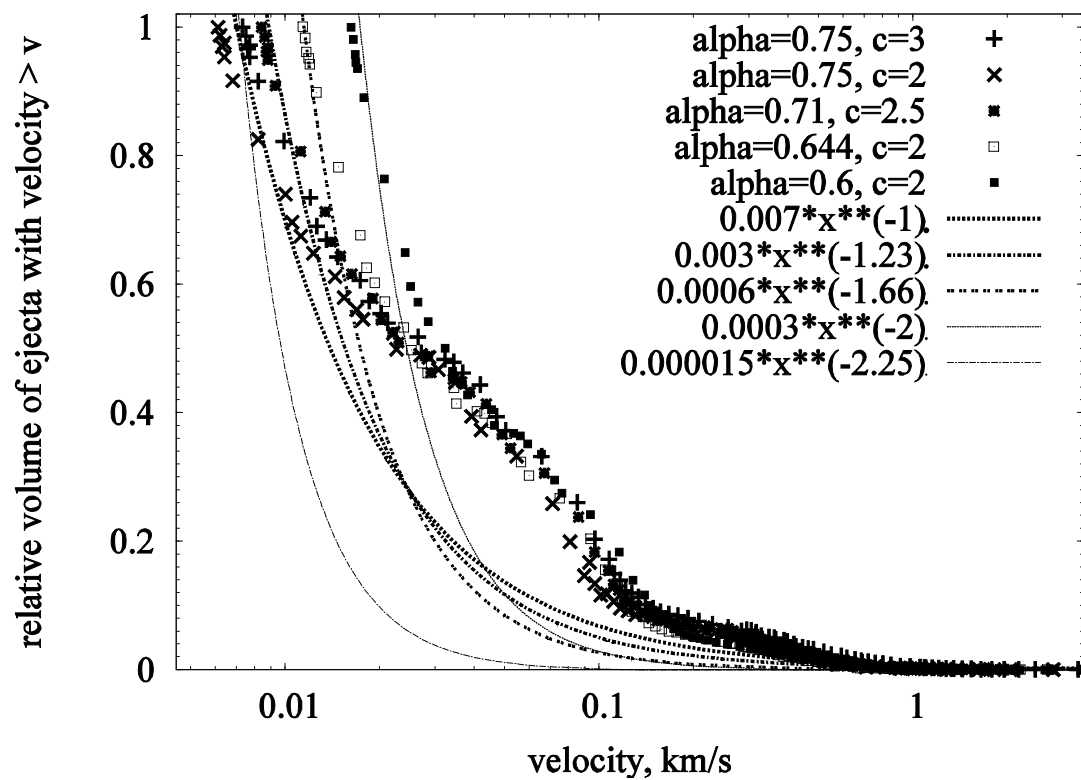


Figure 16

